

APPLICATION OF THE EM27/SUN FTIR SPECTROMETER FOR OPEN-PATH MEASUREMENTS OF CARBON DIOXIDE

Master Thesis
submitted by

Uyen Nguyen

Matriculation Number: 2386438

At the Institute of Meteorology and Climate Research - Atmospheric
Trace Gases and Remote Sensing (IMK-ASF)

First Examiner:	Prof. Dr. Johannes Orphal
Second Examiner:	Priv. Doz. Dr. Andreas-Neil Unterreiner
Supervisors:	Priv. Doz. Dr. Frank Hase Carlos Alberti

Abstract

The anthropogenic emissions of carbon dioxide (CO₂) have been contributing greatly to the greenhouse effect and cause a considerable impact on the Earth's climate system. To improve our predictions and understanding of the future environmental system, the ground-based remote sensing technique has been applied for the long-term observations of atmospheric GHGs. The Collaborative Carbon Column Observing Network (COCCON) was then initiated for validating and supporting the satellite observations, alongside its superior, the Total Carbon Column Observing Network (TCCON). This network is well-known for the use of many portable EM27/SUN Fourier Transform Infrared (FTIR) spectrometers, which is beneficial in determining the local source and sink emissions on a regional scale.

As EM27/SUN spectrometer uses the Sun as its main light source for measuring the GHGs, this thesis enables open-path observations during the night-time and under overcast conditions. A simple optical setup, including an additional incandescent light source and an off-axis mirror, was implemented for testing the first CO₂ open-path measurements on a meter pathlength for three days. The open-path retrievals were then compared with the Integrated Carbon Observation System (ICOS) network to assess the quality and accuracy of the open-path setup, which show a bias of $(0.8 \pm 0.03) \%$ for the fixed ILS parameters. The hypothetical error sources that might contribute to the difference were studied, but the main cause is believed to be the present of noise level and the weak signal intensity of the target CO₂ band.

This work also addresses the disadvantage of applying manmade light source for the long pathlength measurements. Due to the small beam size supported by the source unit, as well as its low brightness, the spectrometer's FOV would not be able to capture the homogeneous image of the source with increasing distance, lowering the signal-to-noise (SNR) ratio of the recorded spectra. By integrating the telescope system into the scheme, the overall magnification of the optical setup would be improved, allowing one to realize longer pathlength with higher SNR. The thesis experimentally demonstrated this effect using the Vixen refracting telescope system.

A reflecting telescope is recommended for future open-path measurements since it realizes twice the pathlength longer than the original distance offered by a refracting system. The measurement noise is lower with increasing area of the primary mirror and source's brightness. A broadband, near-infrared light-emitting diode (LED) is suggested as well, as it requires less power to operate but still provides the same brightness as an incandescent source. It is speculated that the use of a reflector and LED source can deliver higher long-term efficiency and a much better SNR quality than a refracting telescope.

Contents

Abstract	iii
List of Abbreviations	III
List of Figures	V
List of Tables	VIII
1 Introduction	1
2 Theoretical Background	6
2.1 The Earth's atmosphere.....	6
2.1.1 Vertical Atmospheric Composition	6
2.1.2 The Earth's Radiation Budget and The Greenhouse Effect.....	9
2.2 Infrared (IR) spectroscopy	11
2.2.1 Fundamentals of Infrared (IR) Absorption Spectroscopy	11
2.2.2 Molecular Vibration-rotation Spectroscopy	13
2.2.3 Carbon Dioxide (CO ₂)	17
2.3 Molecular Intensity and Line Shape.....	20
2.3.1 The intensity of Spectral Lines.....	20
2.3.2 Natural Linewidths.....	20
2.3.3 Collision Broadening.....	21
2.3.4 Doppler Broadening.....	21
2.4 Fourier Transform Infrared spectroscopy.....	23
2.4.1 Concept of Fourier Transformation	23
2.4.2 Fourier Transform mathematics	25
2.4.3 Computation of FTS Spectral Features	26
3 Instrument and Data Analytical Method	30
3.1 Fourier Transform Infrared EM27/SUN FTIR Spectrometer	30
3.2 Light Source and Path-Extension Strategy	31
3.3 Atmospheric Retrieval Strategy	35
3.4 Computation of Column-averaged Dry-air-mole Fractions	35
4 Ground-based CO₂ Measurement Sessions	37
4.1 Indoor Session: full weekend measurement from the 27th of May 2022 to the 29th of May 2022	37
4.1.1 Measurement Setup	37

4.1.2	Instrumental Line Shape (ILS) selection for Data Analysis.....	38
4.1.3	Intraday Variable of Path-Averaged Temperature and Pressure measurements	39
4.1.4	CO ₂ Concentration Retrievals	40
4.2	Outdoor Session: weekday measurement on the 12 th of August 2022	44
4.2.1	Measurement Setup	44
4.2.2	Measurement Results.....	45
5	Discussion.....	47
5.1	Error Budgets for Open-path CO ₂ Measurements.....	47
5.2	Possible Further Improvements on the Optical Setup.....	50
5.2.1	Telescope.....	50
5.2.2	Light Source	51
6	Conclusion.....	52
7	Declaration of Academic Integrity.....	54
	Bibliography.....	V

List of Abbreviations

Ar	Argon
BS	Beam splitter
CO₂	Carbon Dioxide
CO	Carbon Monoxide
CRDS	Cavity ring-down spectrometer
FOV	Field of view
FTIR	Fourier Transform Infrared
FTS	Fourier Transform Spectrometer
GHG	Greenhouse gas
GOSAT	Greenhouse Gases Observing Satellite
HeNe	Helium-Neon
HCl	Hydrogen Chloride
IR	Infrared radiation
ILS	Instrumental Line Shape
ICOS	Integrated Carbon Observation System
KIT	Karlsruhe Institute of Technology
LED	Light-emitting diode
LOS	Line of sight
CH₄	Methane
ME	Modulation efficiency
OCO	NASA's Orbiting Carbon Observatory
N₂	Nitrogen

N₂O	Nitrous oxide
OPD	Optical path difference
O₂	Oxygen
O₃	Ozone
PE	Phase error
PBL	Planetary boundary layer
RMS	Root-mean-square
TCCON	Total Carbon Column Observation Network
UV	Ultraviolet radiation
H₂O	Water
HDO	Water's deuterated isotopologue
ZPD	Zero-path difference

List of Figures

Figure 1.1. The increase of CO ₂ and CH ₄ concentration since the pre-industrial period until now. The data is given by the Mauna Loa Observatory.....	2
Figure 2.1. Vertical variations of pressure and temperature in the atmosphere at different heights. This represents the steady-state atmosphere and its vertical structure (Kshudiram, 2008).....	8
Figure 2.2. Simplified models of the climate system, adapted from Ponater et al., (2012). The left panel is a one-model system which assumes Earth has no atmospheric layers and only has solar insolation. The right panel is a two-model system including the atmosphere.....	10
Figure 2.3. Electromagnetic spectrums with corresponding molecular motions (Harris 2015)....	12
Figure 2.4. The potential energy curve and energy level between an ideal harmonic system (dash curve) and a realistic graphical demonstration with an anharmonic effect (Hollas, 2004).	14
Figure 2.5. The schematic illustration of the molecular vibration-rotation spectral bands and their transitions are depicted accordingly. The P- and R-branches are responsible for all transitions that yield $\Delta J = -1$ and $\Delta J = +1$ respectively, while the Q-branch consists of all lines with $\Delta J = 0$ and do not appear in the case of parallel bands. The spectrum consists of all resulting branches and locates at a certain wavenumber range making up a specific “band” (Atkins & Paula, 2014).	17
Figure 2.6. Illustration adapted from Atkins & Paula (2014) showing four normal vibration modes of CO ₂ . Modes ν_1 and ν_3 are symmetric and asymmetric stretch, while mode ν_2 describes bending motion in-plane and out-of-plane.	18
Figure 2.7. Simulated transition intensity of CO ₂ (isotopologues was ¹² C ¹⁶ O ₂) absorption band 20012←00001 centred at 4978 cm ⁻¹ . There is a small overlap with another band 21112←01101 at 4965.3851 cm ⁻¹ which was included in the HITRAN database.	19
Figure 2.8. Demonstration of collision (Lorentzian) and Doppler (Gaussian) broadenings. Lorentzian profile (red, grey, and blue) represents frequency shifts due to different motions of emitting molecules (Schrodin 2018).	22
Figure 2.9. Schematic sketch of the standard Michelson interferometer. OPD between the interfering wavefronts is zero when the movable mirror reaches the zero-path difference (ZPD) positions (Eismann, 2012).....	24
Figure 2.10. Interferograms of monochromatic versus polychromatic source, modified and adapted from Stuart (2004).....	25
Figure 2.11. The figure adapted and modified from Siesler et al. (2002) represents the apodization model of boxcar (a1), triangular (b1) and Happ-Genzel (c1) functions. (a2), (b2) and (c2) are the corresponding ILS functions respective to the used apodization model.	27
Figure 2.12. Example of reconstruction spectra of CH ₄ modified and adapted from Eismann (2012), where the left-hand and right-hands sides are without and with apodization.	28

Figure 2.13. The demonstration adapted from Hase et al. (1999) shows two main factors used for describing the deviation of the actual ILS from its ideal shape. The ILS amplitude is broadened when the ME is smaller than 1 and is narrowed when the ME is larger than 1. The value 0 of the PE represents the symmetry of the ILS shape and a PE value that is larger than 0 would result in ILS asymmetry.29

Figure 3.1. The left panel is the top view of the current EM27/SUN spectrometer. The right panel depicts the schematic drawing of the light propagation path coming from the polychromatic source and entering the spectrometer through its housing entrance.30

Figure 3.2. The Left and right figures demonstrate the internal structure on both sides of the source unit.32

Figure 3.3. Adapted from Gisi et al., (2012), this figure demonstrates the solar disk’s image onto the field stop of EM27/SUN (left panel, larger field stop, narrower FOV) and by IFS125HR (right panel, smaller field stop, wider FOV) spectrometers. The blue circles are applied by CamTracker to maintain tracking precision.32

Figure 3.4. The completed diameter of the spectrometer’s field stops is fully illuminated by the source’s image (i.e., orange light).35

Figure 4.1. The top right and left panels are pictures of the spectrometer and light source taken during the measurement. The bottom panel is the schematic drawing of the setup where CO₂ concentrations were measured in between the optical pathlength.....38

Figure 4.2. Left panel: the calculated open-path pressures and ICOS ground pressures. Right panel: temperature measured directly by ICOS tower (140 m a.s.l red) and spectroscopically derived temperature [LINEFIT fitting algorithm of mode 4 (134 m a.s.l, dark cyan) and mode 3 (134 m a.s.l, blue). The experimental and reference difference is illustrated by olive green (mode 4) and orange (mode 3) lines].....40

Figure 4.3. Illustration of three-days averaged band intensity of CO₂ in the spectral window with centred wavenumber at 4978 cm⁻¹ and the fit. Residual plots from modes 4 and 3 were multiplied by a factor of 100 to show their detailed structure.41

Figure 4.4. The comparison of XCO₂ concentration between open-path EM27/SUN and ICOS spectrometer, along with their differences stated in the top panel.42

Figure 4.5. Wind speed and wind direction are plotted against the XCO₂ difference between the two modes.43

Figure 4.6. Fluctuated ME and PE values generated by the LINEFIT algorithm of mode 3 for all time points.....43

Figure 4.7. With the insertion of the telescope system, the spectrometer’s FOV is illuminated fully by the source at distance farther than the initially speculated pathlength in section 3.2.....44

Figure 4.8. The optical setup with a telescope system in between the spectrometer (left) and the light source (right) for CO₂ open-path measurement.45

Figure 4.9. Spectroscopic spectrum-derived temperatures (left panel) and the calculation of dry-air-mole XCO ₂ fractions (right panel).....	46
Figure 4.10. Spectra and residual signals of each measurement hour.....	46
Figure 5.1. XCO ₂ comparison between the EM27/SUN spectrometer with the ICOS CRDS.....	48
Figure 5.2. The proposed setup for open-path EM27/SUN for achieving longer pathlength.	51

List of Tables

Table 1. Summary of the calculated open-path pressures based on ICOS reference pressures and relevant wind information.	45
Table 2. Leading error sources that influence the retrieved CO ₂ mole fractions for the full weekend session. To assess the impact of the pathlength, temperature, pressure, HITRAN's line intensity and pressure broadening uncertainties on the analytical results, XCO ₂ values of all hours were recalculated based on the change, analysed under mode 4 and 3 strategies, and compared with the original open-path XCO ₂ concentrations.	49

1 Introduction

A continual study of Earth's atmosphere, its structure and composition is crucial for achieving a proper understanding of the impact of human-related activities on global environmental change. Among numerous research activities in this area, monitoring the concentrations of atmospheric trace gases released into the atmosphere every day is an indispensable mission. Accurate measurements improve our understanding of anthropogenic emissions, our ability to predict future climate and the effectiveness of mitigation strategies. Various comprehensive and well-known techniques of detecting and quantifying those gases such as satellite observations, in-situ and ground-based remote sensing measurements contribute to this effort. In combination with model investigations, they allow the determination of source and sink locations, the finding of direct correlation between greenhouse gases (GHGs) and manmade factors (Alberti et al., 2022), as well as the careful analysis of the mechanism of the global carbon cycle (Friedlingstein et al., 2022).

The greenhouse effect is the result of heat being trapped by a certain type of gases in the atmosphere, hence those are named the GHGs which can come from either natural sources (e.g., respiration, plant decomposition, venting volcanoes...) or human causes (agriculture, deforestation...). The current steady rise of the atmospheric carbon dioxide (CO₂) concentration is mainly due to the use of fossil fuels, making it the greatest contributor to the global gas emission of roughly 64 % by 2019 (Skea et al., 2022). During the pre-industrial period from 1750 to 1850, the concentration of atmospheric CO₂ was estimated to be 278.3 ± 2.9 parts per million (ppm) and 285.5 ± 2.1 ppm, respectively (Gulev et al., 2021). Nowadays, in the year 2022, the Mauna Loa Observatory records the current CO₂ value to be around 420.99 ppm¹, being equivalent to a rise of 50 % since the beginning of the industrial era. Furthermore, fugitive emissions of methane (CH₄) which is the second most active greenhouse factor from the production, transportation and distribution of fossil fuel should be taken into consideration as well. Being 21 times more potent at trapping heat in the atmosphere than CO₂, the anthropogenic rise of CH₄ level is a dangerous threat despite the fact that its lifetime is shorter and its global emission is lower than CO₂ (Haradhan, 2011). The global mean of CH₄ was measured to be 729 ± 9.4 parts per billion (ppb) in 1750, then to be approximately 807.6 ± 13.8 ppb in 1850 (Gulev et al., 2021) and to currently reach the value of 1908.5 ppb² at 161.85 % increase as of today. Because the dominant emissions are from both gases, the Earth's surface temperature has reached 1.5 °C since the pre-industrial era³.

¹ <https://gml.noaa.gov/ccgg/trends/>

² https://gml.noaa.gov/ccgg/trends_ch4/

³ <https://www.ipcc.ch/sr15/>

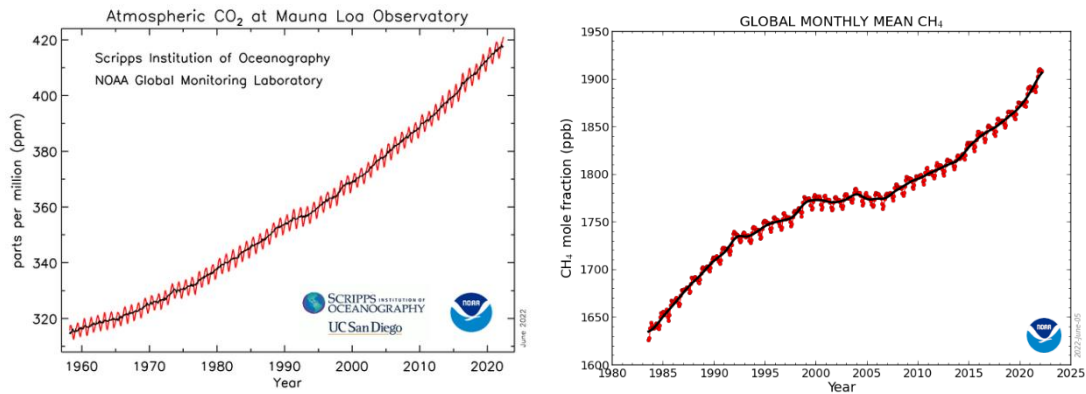


Figure 1.1. The increase of CO₂ and CH₄ concentration since the pre-industrial period until now. The data is given by the Mauna Loa Observatory.

In principle, the greenhouse effect is essential to sustain life on Earth. Without it, the Earth's average temperature would be -30 °C instead of 15 °C as recorded nowadays (Khan, 2017). However, the alarming rate of increasing trace gas concentration adversely impacts the balance of the climate system. This unnatural enhancement of the greenhouse effect leads to global warming. For instance, the rise in sea-level and extreme weather events are two of the main direct consequences of this outcome (Khan, 2017; Jain, 1993). The increase of sea- and ocean-levels are the result of the accelerated temperature and the excess of trapped heat that melt snow and ice from either polar ice sheets or mountain glaciers. As the level has escalated by roughly 18 cm in the last 100 years, it is predicted that 90 cm of sea-level could be reached by the year 2100, which would be a global catastrophe. A number of populations who live in low-lying coastal cities or islands are now already facing the potential threat of losing their home and having to relocate to higher ground. Moreover, due to the rapid rise of average temperature, extreme weather events such as severe drought can frequently occur at a higher rate, causing problematic damage to agriculture, global food security, and the lack of clean water resources. This unusual sudden change would also leave some areas uninhabitable, leading to the extinction of some species and insects as well (Haradhan, 2011).

Over the past few years, several attempts of reducing greenhouse emissions were tackled by numerous international organizations. In 2015, the universal protocols of limiting the global warming temperature to 1.5 °C were delivered at the United Nations Climate Change Conference held in Paris, where 196 parties around the globe agreed to join hands (Paris Agreement¹). Along the path, numerous programs and studies were performed to improve the scientific interpretations on the current state of climate change and its effect on our ecosystem, as well as the overall understanding of the global carbon cycle. For these specific purposes, long-term observations of

¹ https://unfccc.int/sites/default/files/resource/parisagreement_publication.pdf

atmospheric GHGs are demanded, which can be conducted by the three sophisticated methods of satellite, in-situ, and ground-based remote sensing techniques. Each has its pros and cons. In-situ measurements provide extremely high accuracy (Alberti et al., 2022) and are perfect for measuring the GHG concentrations near the surface (Boesch et al., 2021), but were also indicated by various studies in the past to deliver inconsistent results when compared to other total column measurements (Warneke et al., 2010). The uncertainties of this method are associated with the description of the vertical exchange, which is mediated by the atmospheric turbulence in the planetary boundary layer (PBL) (Kretschmer et al., 2012). For the other techniques, both satellite and ground-based remote sensing performance measure the column-averaged abundances of the target gases in Earth's atmosphere. Satellite observations offer quasi-global coverage but suffer from the uncertainties introduced by the complicated radiative transfer of the nadir geometry, the noise level achieved, and limited spatial resolution or sampling density. Ground-based solar absorption measurements achieve reference accuracy and precision, therefore are essential for the validation of satellite sensors. Mobile spectrometers can even be used for the study of local sources. The similar disadvantage between the ground-based and in-situ networks is that both suffer from sparse coverage at the moment, otherwise, the remote sensing technique delivers much higher representativeness than the in-situ method.

In recent years, numerous space-borne missions were put in operation, such as the Greenhouse Gases Observing Satellite (GOSAT¹) and NASA's Orbiting Carbon Observatory (OCO-2²/OCO-3³) for measuring the column-averaged dry air CO₂ mole fraction. To validate and support those observations, a network of ground-based solar absorption Fourier Transform Infrared (FTIR) spectrometers operating in the near-infrared region was initiated, named the Total Carbon Column Observation Network (TCCON⁴). Together with the Integrated Carbon Observation System (ICOS⁵) network, which delivers highly accurate reference in-situ observations of GHGs and the carbon fluxes between the domains of the atmosphere, ecosystem, and ocean, TCCON and ICOS have greatly contributed to the improvement of the assessment of the annual CO₂ and CH₄ emissions from the complex environmental settings. However, the TCCON network has some disadvantages. Although its high-resolution IFS125HR spectrometer offers outstanding precision, reference quality and high stability during operation, being a high-cost and cumbersome device is a fair trade-off for those benefits. Having a very large dimension and a mass of more than 100 kg, the IFS125HR spectrometer requires a tremendous amount of infrastructure to be operated (e.g., stable support platform...) and expert maintenance on site (e.g., realignment...). The world

¹ <https://www.gosat.nies.go.jp/en/>

² <https://ocov2.jpl.nasa.gov/>

³ <https://ocov3.jpl.nasa.gov/>

⁴ <https://tcon-wiki.caltech.edu/Main/TCCON>

⁵ <https://www.icos-cp.eu/>

distribution of IFS125HR stations of the TCCON network is not enough to conduct the GHG measurements on an even global coverage (Sha et al., 2020). It is also nonsensical, time-consuming, and inconvenient to relocate the huge instrument to a new desired destination, which can be unmanageable on a campaign basis in some remote areas (Gisi et al., 2012; Frey et al., 2019) and cause many difficulties in determining and observing the isolated location of sources and sinks on a regional scale (Frey et al., 2015).

In 2012, a solar absorption spectrometer called EM27/SUN developed by the Karlsruhe Institute of Technology (KIT) in cooperation with Bruker provided the solutions to the aforementioned downsides. Being a portable, robust, economical, and light-weight device, the resulting low-resolution EM27/SUN FTIR spectrometer is a great choice for characterizing the local sources and sinks and can be used in all types of field campaign, even on a continuous moving ship (Frey et al., 2015). The spectrometer has been proved and confirmed by various studies and field campaigns to deliver not only excellent stability, long-term performance, and deployment, but also reliable results with high precision and accuracy as compared to the reference highly qualified data of TCCON (e.g., Gisi et al., 2012; Hase et al., 2015; Chen et al., 2016; Hedelius et al., 2016; Sha et al., 2020; Jones et al., 2021...). Currently, there are more than 40 EM27/SUN instruments that are operated by different working groups around the globe (e.g., Germany, USA, UK, India, Namibia, Japan, China, and Mexico), forming a new emerging network of COllaborative Carbon Column Observing Network (COCCON¹). The network consisting of several portable and easy-to-deploy EM27/SUN instruments is a crucial complementary of TCCON, which helps to maintain and increase the long-term GHG measurements and observations, improve the GHG estimations, as well as to contribute to further understanding of the regional sources and sinks (Frey et al., 2019).

Since the EM27/SUN spectrometer uses the Sun as a direct light source, measurements can only take place under sunny condition. Therefore, this thesis aims at enabling open-path observations for measuring the local CO₂ concentration during the night-time and on cloudy days. The open-path approach with the use of an additional light source has been performed for different research purposes. For example, it can be used to characterize the instrumental line shape (ILS) in order to minimize the systematic errors in the trace gas retrievals introduced by the imperfect ILS (Frey et al., 2015; Alberti et al., 2022). The open-path method is also advantageous for deducing the spatially averaged concentrations of the target gases in complex small-scale urban and regional environments (Griffith et al., 2018; Deutscher et al., 2021). Through the integration of over kilometre-length scale, spatial averaging can determine the strength of localised source and sink emissions of GHGs that are less sensitive to small-scale variability. As the first step of this research,

¹ <https://www.imk-asf.kit.edu/english/COCCON.php>

the three main objectives are to (1) construct an optical configuration that supports the open-path measurement on the order of tens to hundreds of meters, (2) evaluate the reliability of the open-path results on the daily cycle of CO₂ by comparing with the reference measurements given by the ICOS tower in Karlsruhe, and (3) suggest further improvements for the applied optical setup to enhance the quality of the open-path measurement in the future research.

2 Theoretical Background

2.1 The Earth's atmosphere

This section focuses on reviewing the theory of Earth's atmosphere and the fundamental aspects of greenhouse effect. The first subsection studies the Earth's composition and its vertical structure, while the second subsection emphasizes the important key driver for Earth's climate system, radiation budget and how it is connected to the greenhouse effect. The content of this section was mostly adapted from Kshudiram (2008), Meerkötter & Vázquez-Navarro (2012), and Ponater et al. (2012).

2.1.1 VERTICAL ATMOSPHERIC COMPOSITION

Due to the lack of well-founded evidence, one can only hypothesize that the formation of our atmosphere, as well as the origin of Earth as a planet in the solar system, began 4.6 billion years ago under the influence of a cosmic event called the Big Bang. The primordial atmosphere in the early stage is speculated to mainly consist of hydrogen and other gases with trace amounts. It is believed that there was no free oxygen molecule to support life at all at this time. The Earth then started to cool down to the point where the complex chemical reactions in the Earth's crust interacted with the primordial atmosphere to form a new atmospheric state, supporting the earliest life forms on Earth known as the single-celled microbes. Under the presence of water and sunlight, they consumed carbon dioxide and liberated oxygen into their surrounding through a bio-chemical photosynthesis process. The aggregation of oxygen in the atmosphere led to numerous historical evolutions and developments of a more complex life form, eventually evolving into the current life form that we observe now. Research estimates that it took approximately one billion years for the Earth's atmosphere to slowly stabilize into its current state as of today.

Nitrogen (N_2), oxygen (O_2) and argon (Ar) are the three primary gaseous constituents of the Earth's atmosphere. By volume in dry air, N_2 accounts for the highest percentage of 78.09 %, while 20.95 % and 0.93 % are the proportions of O_2 and Ar, respectively. Due to their long residence times, their concentrations are time-invariant and globally homogeneous. However, unlike these atmospheric dominant abundances whose influence on the climate system is largely neglectable, GHGs from the minor fraction such as water (H_2O), nitrous oxide (N_2O) and ozone (O_3) which serves as pollutants in the troposphere are the utmost important factors in the change of the meteorological processes, apart from the aforementioned CO_2 and CH_4 trace gases. Even though these GHGs only comprise 0.03 % by volume in dry air, have short residence time and vary continuously in space and time, they are the main contributors to the greenhouse effect because of

their interactive capability with infrared (IR) radiation and their thermodynamic property. This is explained in detailed in section 2.2 of this thesis.

Water has been well-known to be one of the most critical substances for functioning life and for detecting the signs of life outside the solar system on exoplanets, yet its present also plays a significant role in the change of atmospheric properties and behaviour on Earth. Water's change of phase between solid, liquid and gas enables its structure to either absorb or release a large amount of heat in the atmosphere, making it a strong GHG aside from CO₂ and CH₄. The condensation of water into clouds and rain is an example of how phase change has directly shaped the current state of our climate system as of today. Since the majority of water vapour present in the atmospheric troposphere, most of the weather phenomenon such as rain and snow takes place in this layer.

In the application of meteorology, the analysis of the structure and behaviour of atmospheric gases is interpreted with simplifying assumptions that are given by the ideal gas model. Air properties such as pressure and temperature are mainly derived and approximated under this law. Atmospheric pressure is the result of the weight of the air vertical column overlying above the target point at a specific altitude level due to the effect of Earth's gravitational pull. Its average value at 0 °C (i.e., mean sea level) is recorded to be 1013 hPa. Temperature is defined as the heat measured in a body. However, the increase in temperature for different bodies depends on not only the quantity of heat that is given to them but also their property, called heat capacity. One can compute the pressure at any atmospheric height z using the equation of state $p = \rho RT$ under the Hydrostatic equilibrium assumption:

$$\delta p = -\rho \cdot g \cdot \delta z = -\left(\frac{p}{R \cdot T}\right) \cdot g \cdot \delta z \quad (2.1)$$

Here, ρ is the mean density of air, R is the gas constant, T is the temperature and g is the gravitational acceleration. Eq. (2.1) enables one to determine the pressure at the target height if the ground pressure at the Earth's surface is known:

$$p(z) = p_0 \cdot \exp\left(-\frac{g \cdot z}{R \cdot T_0}\right) = p_0 \cdot \exp\left(-\frac{z}{H}\right) \quad (2.2)$$

$H = \frac{R \cdot T_0}{g}$ is preferred as scale height and p_0 is the pressure at the ground level. The estimated value of H is determined in studies depending on the considered constant T_0 . At $T_0 = 288$ °K, H has a value of 8434 m. However, Eq. (2.2) is only applied when the temperature T at a certain height z is assumed to be constant and is the same as the surface temperature T_0 . Therefore, the actual equation used for calculating the pressure in this study is defined in Eq. (2.3), where the height difference between the ground level and the target altitude above sea level (a.s.l) is added as $\Delta h = z - z_0$ and the scale height at z in the denominator is rearranged as $H_z = \frac{H(T_0) \cdot T_z}{T_0}$. In this thesis, the

ground pressure p_{ICOS} and the ground temperature T_{ICOS} given by the ICOS reference tower at the corresponding scale height $H(T_{ICOS})$ were used to calculate the pressure at target height z .

$$p(z) = p_{ICOS} \cdot \exp\left(-\frac{\Delta h}{H_z}\right) = p_{ICOS} \cdot \exp\left[-\frac{z - z_{ICOS}}{H(T_{ICOS}) \cdot T_z} \cdot T_{ICOS}\right] \quad (2.3)$$

Both pressure and temperature of air vary in space and time, hence an exact set of their values at different heights aloft is difficult to achieve. Fig. 2.1 illustrates the mean vertical distribution of atmospheric temperature and pressure at certain heights, where the pattern shows that the pressure increases nearly exponentially with the decrease of height, while the temperature fluctuates in a haphazard manner.

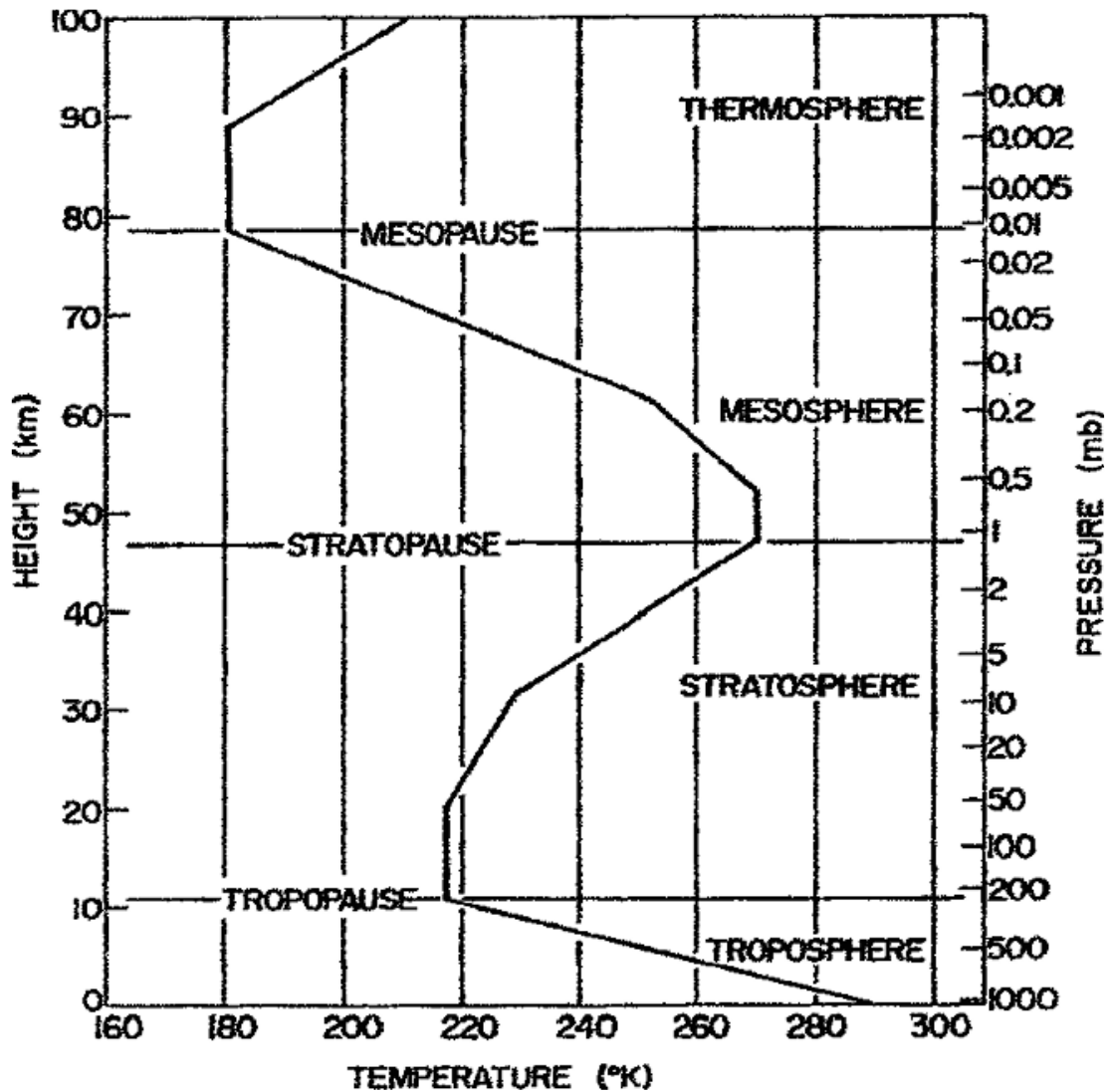


Figure 2.1. Vertical variations of pressure and temperature in the atmosphere at different heights. This represents the steady-state atmosphere and its vertical structure (Kshudiram, 2008).

The Earth's atmosphere is divided into four principal layers: the troposphere, the stratosphere, the mesosphere, and the thermosphere. The troposphere is the lowest layer, which extends from the

surface to between the height of 9 km at the poles and a height of 16 km at the equator. Fig. 2.1 first demonstrates the temperature, which starts to decrease from around 15 °C at 0 km with a rate of 6.5 °C per km until it reaches the tropopause level. This is the consequence of the adiabatic cooling upon volume expansion caused by the pressure drop as one goes higher up in altitude. As the thermal radiation from the Earth's surface is absorbed by the molecules in this layer, convection and turbulent transfer of heat are induced, maintaining the temperature distribution. The troposphere is followed by the stratosphere layer, where the temperature rises gradually until 0 °C due to the large number of O₃ molecules that this layer carries. The Sun's ultraviolet (UV) rays are mostly absorbed by the structure of O₃ atoms in the atmospheric stratosphere, alongside N₂ and O₂ mixtures which create a shield and protect the life on Earth from the perilous short-wavelength radiations. Contrary to the troposphere, the small amount of water vapour and the increase in temperature prevent a good vertical mixing in the stratosphere. Above the stratosphere lies the mesosphere where the temperature again decreases for the same reason as observed in the troposphere. However, after reaching the mesopause level, the temperature escalates to a great extent with altitude when entering the thermosphere layer. This is due to the strong interaction between the Earth's majority molecules and highly charged radiations from space, where O₂ and N₂ absorb the high-energy short-wavelength rays and get ionized.

2.1.2 THE EARTH'S RADIATION BUDGET AND THE GREENHOUSE EFFECT

As the energy budget of the Earth's atmosphere and surface is governed by its energy exchange with external solar and internal thermal radiations, the radiation budget is a critical driving force for the planet's climate system and is involved in various physical and chemical processes in the atmosphere. Since the Earth continuously receives solar energy on a long-term and global-averaged scale, the radiation budget is regarded as being in equilibrium and describes the overall energy balance between the incoming solar radiation and the outgoing longwave thermal, or the reflected shortwave energy from the Earth's atmospheric components. The total amount of solar radiation that Earth receives can be calculated based on its cross-section πR_E^2 , where R_E is the Earth's radius. Due to the planet's rotation, the energy is distributed across the planet's surface area of $4\pi R_E^2$. Assuming the light waves enter under different angles and considering the fact that half of the planet does not receive this energy during the night-time, the averaged incoming solar energy is equivalent to one-fourth of the solar constant, which is defined as the irradiance of solar energy at the top of Earth's atmosphere and is estimated to be $1365 \frac{\text{W}}{\text{m}^2}$. This means the annual average of the total solar irradiance (i.e., $341 \frac{\text{W}}{\text{m}^2}$) is responsible for all interactions and energy conversion in the climate system. Due to the backscattering and reflection, it is approximated that the energy flux of $102 \frac{\text{W}}{\text{m}^2}$ escape at the top of the atmosphere, leaving a total net gain of $239 \frac{\text{W}}{\text{m}^2}$ solar radiation to be absorbed by the Earth's surface and its atmospheric layers.

In thermal equilibrium, the Earth absorbing the additional solar energy and re-emitting them correspondingly can be described as a mathematic blackbody model, which was proposed by Max Planck in 1900 as a function of temperature and wavelength:

$$B(\lambda, T) = \frac{2 \cdot h \cdot c^2}{\lambda^5 \left(e^{\frac{h \cdot c}{\lambda \cdot k_B \cdot T}} - 1 \right)} \quad (2.4)$$

Here, h is the Planck's constant and has the value of 6.626×10^{-34} Js, c is the speed of light and has a constant value of $2.998 \cdot 10^8 \frac{m}{s}$, λ represents wavelength, k_B of $1.38 \cdot 10^{-23} \frac{m^2kg}{s^2K}$ illustrates the Boltzmann constant and T is the temperature. Integrating this spectral equation over the hemisphere and all wavelengths will result in the Stefan-Boltzmann law, which states the total irradiance emitted by a blackbody is proportional to the fourth power of its temperature:

$$E = \varepsilon \cdot \sigma \cdot T^4 \quad (2.5)$$

Where $\sigma = \frac{2\pi^5 \cdot k_B^4}{15 \cdot h^3 \cdot c^2} = 5.67 \cdot 10^{-8} \left(\frac{kg}{s^3 \cdot K^4} \right)$ is defined as the Stefan-Boltzmann constant and ε is the emissivity ($\varepsilon = 1$ for blackbody). The atmosphere is the main factor for maintaining the radiation balance and is also responsible for the temperature today. An increase of energy gain on the surface occurs when the active atmospheric GHGs absorb either incoming solar energy or energy released from the Earth's surface, then thermally re-emit the received energy at the corresponding wavelength region, consequently rising the global averaged temperature. To illustrate this effect as a part of Earth's radiation budget and to emphasize the role of the atmosphere, two simplified models of Earth's global climate system are demonstrated below:

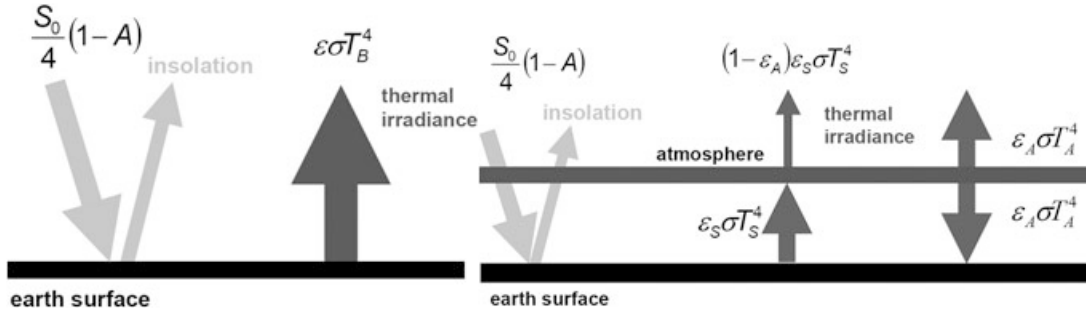


Figure 2.2. Simplified models of the climate system, adapted from Ponater et al., (2012). The left panel is a one-model system which assumes Earth has no atmospheric layers and only has solar insolation. The right panel is a two-model system including the atmosphere.

Based on Eq. (2.5), the one-model system can be written as in Eq. (2.6) such that the Earth's radiation budget is in equilibrium:

$$(1 - A) \cdot \frac{S_0}{4} = \varepsilon_S \cdot \sigma \cdot T_S^4 \quad (2.6)$$

Here, $A \approx 30\%$ is the planetary albedo indicating the reflective fraction of the outgoing solar irradiance, S_0 is the solar constant and ε_S is the emissivity of the Earth's surface. Based on Eq. (2.6), assuming A is 0.3, S_0 is $1365 \frac{\text{W}}{\text{m}^2}$ and ε_S is 0.95, one would theoretically obtain a surface temperature of $258 \text{ }^\circ\text{K}$ ($\sim -15 \text{ }^\circ\text{C}$). On the other hand, the two-model system is described by Eq. (2.7) as a function of two unknown atmospheric temperature T_A and surface temperature T_S :

$$\begin{aligned} (1 - A) \cdot \frac{S_0}{4} + \varepsilon_A \cdot \sigma \cdot T_A^4 &= \varepsilon_S \cdot \sigma \cdot T_S^4 \\ (1 - \varepsilon_A) \cdot \varepsilon_S \cdot \sigma \cdot T_S^4 + 2 \cdot \varepsilon_A \cdot \sigma \cdot T_A^4 &= \varepsilon_S \cdot \sigma \cdot T_S^4 \end{aligned} \quad (2.7)$$

T_A and T_S can be analytically calculated based on reasonable assumptions for the emissivity of the atmosphere ε_A and surface ε_S . With the same aforementioned parameters and the assumption that ε_A is 0.75, T_S and T_A can be calculated to be $287.15 \text{ }^\circ\text{K}$ ($\sim 14 \text{ }^\circ\text{C}$) and $240.15 \text{ }^\circ\text{K}$ ($\sim -33 \text{ }^\circ\text{C}$). Although these values are derived from the simplified models, they are in good agreement with the global mean temperature values observed by satellite and in-situ measurements. Needless to say, without the presence of the atmosphere, life on Earth would not have happened as of today.

2.2 Infrared (IR) spectroscopy

In this section, the fundamentals of spectroscopy are discussed. The first subsection gives an overview of light-matter interaction, which relates to three main kinds of transitions (i.e., electronic, vibrational, and rotational) in a molecule. Here, the impact of infrared (IR) radiation on different structures of GHGs is primarily studied. The second subsection uses the vibrational and rotational energy equations of a diatomic model to explain the formation of the vibration-rotation band. To demonstrate the spectral structure of this transition, the polyatomic CO_2 molecule is specified as an example in the third subsection.

The knowledge of this section is based on the spectroscopy textbooks of Atkins & Paula (2014), Harris (2015) and Hollas (2004).

2.2.1 FUNDAMENTALS OF INFRARED (IR) ABSORPTION SPECTROSCOPY

The field of spectroscopy focuses on understanding the quantized interaction between matter and electromagnetic radiation. The resulting absorption, emission and even scattering spectra are then investigated, which is determined by the spectroscopic structure of the molecule, such as mass and dimensions, strengths of bonds, its dipole moment or its shape. Depending on the energy and wavelength, the electromagnetic spectrum is divided into radio-wave, microwave, infrared, visible, ultraviolet, X-ray and γ -ray, from lowest to highest photon energies as shown in Fig. 2.3. The relationship between energy and frequency of light is given by the Planck's relation: $E = h \cdot \nu = \frac{h \cdot c}{\lambda}$, where E is the photon energy and ν is the light frequency. The higher the photon's energy, the

shorter its wavelength is. In spectroscopy, wavenumber is frequently used more than wavelength, defined as $\bar{\nu} = \frac{1}{\lambda} = \frac{c}{\nu}$.

When a molecule absorbs the incident electromagnetic radiation, it is promoted to a higher excited state and its energy increases accordingly. The energy of a molecule can, contrariwise, decrease through emission, where the molecule relaxes to its original stable ground state and emits a photon simultaneously. Both absorption and emission initiate the processes of change, which are the transitions of the electronic, vibrational, and rotational states in that molecule. These transitions can be illustrated in terms of discrete energy levels (e.g., E_0 is the electronic ground state, E_1 is the electronic first excited state...). However, absorption can only take place when the incident photon energy matches the energy difference between different levels of that molecule ($\Delta E = h \cdot \nu$). Infrared (IR) energy is insufficient to promote electronic transition but is enough to cause vibrational, rotational and vibration-rotation transitions. This is shown in Fig. 2.3, where only some specific motions of a molecule can be observed under certain regions. While microwave and IR radiations stimulate rotations and vibrations of a molecule, electronic transitions between orbitals correspond to photon energies in the visible and ultraviolet regions. Fig. 2.3 also demonstrates that X-rays and shorter-wavelength ranges break the strong chemical bonds between atoms of a molecule, resulting in molecular ionizations.

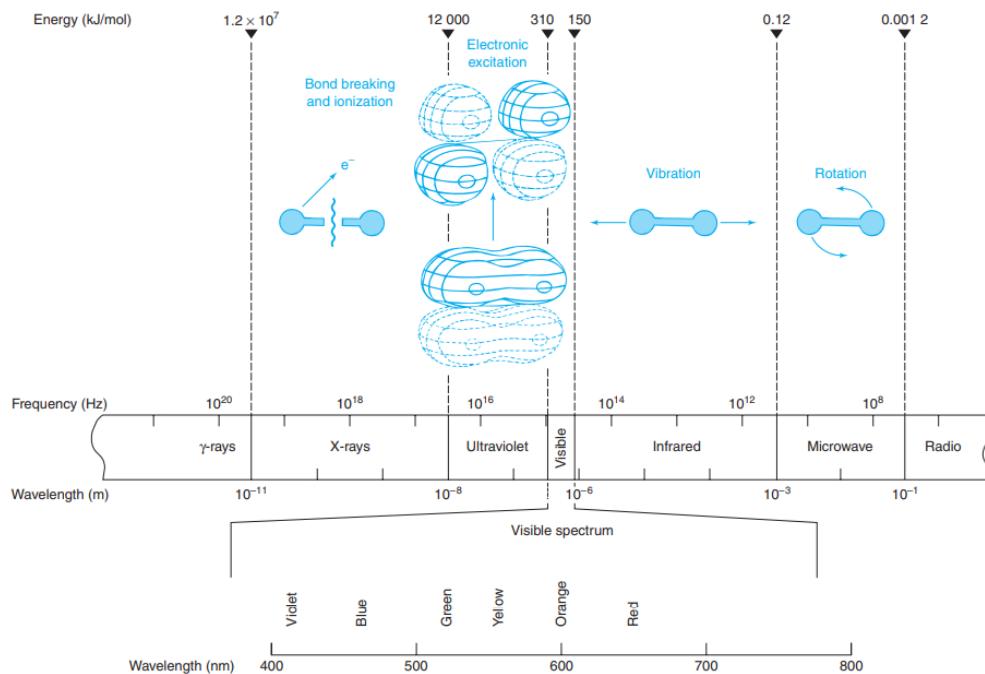


Figure 2.3. Electromagnetic spectrums with corresponding molecular motions (Harris 2015).

IR spectroscopy is an analytical technique that is well-known for identifying molecular structure and properties. It is especially useful in measuring the concentration of atmospheric GHGs. A molecule is said to be infrared-active only when there is a change in its dipole moment induced by

the vibrational motion itself. This condition is specifically related to the selection rule for IR spectroscopy (i.e., harmonic oscillation transition rule). Since the polyatomic GHGs have higher numbers of atoms and bonds, which lead to much richer sets of translational, rotational, and vibrational modes (e.g., asymmetric stretch, bend...) than homonuclear diatomic molecules, they are able to initiate non-zero dipole transition moment based on different mode combinations. This explains how GHGs can efficiently capture the passing IR waves and re-radiate them as heat, consequentially warming the Earth's average temperature. Other atmospheric gases which have a heteronuclear diatomic structure such as carbon monoxide (CO) or hydrogen chloride (HCl) are infrared-active under the same principle as well. On the contrary, having a simple mode of stretching and no change in the dipole oscillation due to the symmetric structure, homonuclear N₂ and O₂ molecules are transparent to the IR photons (i.e., infrared-inactive), hence contributing insignificant impact on the climate system.

IR radiation covers a wavelength range from around 700 nm to 1 mm as shown in Fig. 2.3 and is classified as near-infrared (from 700 nm to 3000 nm), mid-infrared (from 3000 nm to 15000 nm) and far-infrared (from 15000 nm to 1 mm). GHGs absorb IR radiation at different centred wavelengths depending on their molecular transition states, forming absorption bands. While the strong absorption bands of CO₂ and H₂O are mainly observed in the mid-infrared region, some of which with weaker intensity are also found in the near-infrared spectral range. In the context of spectroscopy, the word “band” denotes a spectral structure observed in the absorption spectrum and is associated with certain vibrational transitions. The rotational energy levels give rise to the fine structure of a band, creating groups of individual spectral lines (see Fig. 2.7 as an example for CO₂). A specific band or transition from lower to upper levels can be expressed in terms of quantum numbers (v', J') ← (v'', J''), where v is the vibrational quantum number and J is the rotational quantum number. Different absorption bands of CO₂ located at certain centred wavelengths in the near-infrared region are the result of the overtones and different combinations of vibration-rotation transitions.

2.2.2 MOLECULAR VIBRATION-ROTATION SPECTROSCOPY

The vibration-rotation spectral bands are the transitions from the rotational levels of one vibrational state to the rotational levels of another vibrational state in the same electronic energy level. In quantum-mechanics, the vibrational energy of a diatomic molecule under the approximation of harmonic oscillation is defined as below:

$$E_v = h \cdot \nu \cdot \left(v + \frac{1}{2} \right) = \frac{h}{2\pi} \cdot \left(\frac{k}{\mu} \right)^{0.5} \cdot \left(v + \frac{1}{2} \right) \quad (2.8)$$

In this equation, v = 0, 1, 2... is the vibrational quantum number representing the vibrational states and the frequency ν which can be expanded further in the connection with the force constant k and

the reduced mass $\mu = \frac{m_1 \cdot m_2}{m_1 + m_2}$. In the spectroscopic context, Eq. (2.8) can be re-written in terms of wavenumber $\bar{\nu} = \frac{1}{\lambda} = \frac{E}{h \cdot c}$. Note that the wavenumber is also expressed as ω in some textbooks. Nevertheless, it is denoted here as $\bar{\nu}$ to avoid confusion with the term angular frequency ω .

$$G(v) = \frac{E_v}{h \cdot c} = \bar{\nu} \cdot \left(v + \frac{1}{2} \right) \quad (2.9)$$

In reality, a diatomic molecule is not perfectly well-described by the harmonic oscillator model. Under the assumption of molecular vibrational motion made by Hooke's law, it is only true when one estimates the harmonic behaviour for low vibrational energy states. As the distance between 2 atoms increases, the dissociation energy is approached, causing the potential to differ from the predicted harmonic approximation and consequently resulting in a steeper potential energy curve (see Fig. 2.4). This deviation gives rise to anharmonicity, whose function can be mathematically derived and additionally modified as shown in Eq. (2.10). Note that this equation can be expanded in a power series if there are more anharmonic terms involved in a considered system.

$$G(v) = \bar{\nu} \cdot \left(v + \frac{1}{2} \right) - \bar{\nu} \cdot x_e \cdot \left(v + \frac{1}{2} \right)^2 \quad (2.10)$$

The anharmonic constant is defined as x_e and $D_e \approx \frac{\bar{\nu}}{4 \cdot x_e}$ represents dissociation energy for two transitions. The selection rule for harmonic oscillation requires the vibrational transitions to be either $\Delta v = +1$ (absorption) or $\Delta v = -1$ (emission). However, the anharmonic selection rule relaxes this requirement, where $\Delta v = \pm 1, \pm 2, \pm 3 \dots$ are allowed. The transition from $v = 0$ to $v = 1$ is regarded as the fundamental vibration, whereas higher Δv transitions are referred as overtone bands.

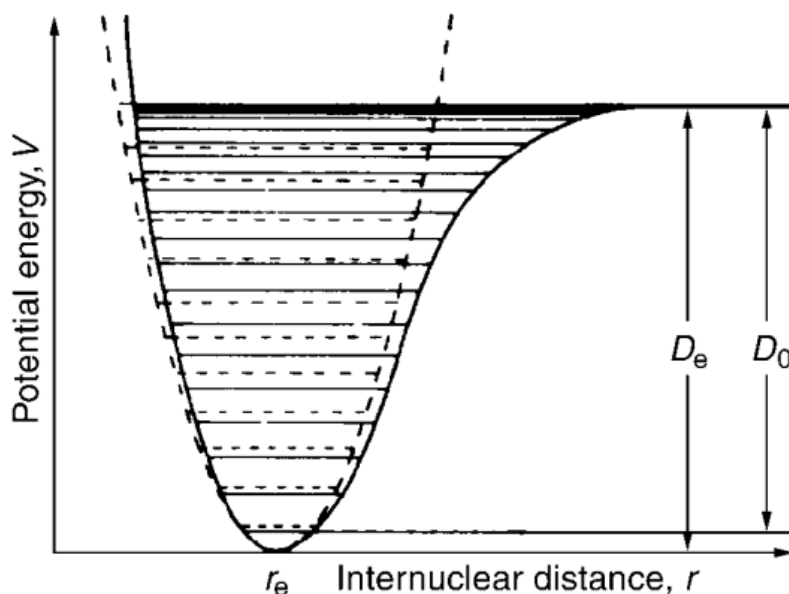


Figure 2.4. The potential energy curve and energy level between an ideal harmonic system (dash curve) and a realistic graphical demonstration with an anharmonic effect (Hollas, 2004).

In addition to the vibrational motion, the rotational energy of a diatomic molecule in relation to the moment of inertia can be written as:

$$E_r = \frac{h}{8\pi^2 \cdot I} \cdot J \cdot (J+1) \quad (2.11)$$

In this equation, $I = \mu \cdot r^2$ is the moment of inertia (r is the distance between two bodies) for diatomic molecules, $J = 0, 1, 2, \dots$ is the total angular momentum quantum number and is the sum of rotational, orbital and electron spin. Eq. (2.11) in terms of wave number can be re-written as in Eq. (2.12), which is related to rotational constant $B = \frac{h}{8\pi^2 \cdot I \cdot c}$:

$$F(J) = \frac{E_r}{hc} = \frac{h}{8\pi^2 \cdot I \cdot c} \cdot J \cdot (J+1) = B \cdot J \cdot (J+1) \quad (2.12)$$

One can treat the target molecules as rigid rotors if there is no distortion due to the rotational stress, thereby neglecting the centrifugal distortion. A molecule has three degrees of freedom connected to the molecular rotational motions in three directions in the Cartesian coordinate system. That is to say, according to the x-, y-, and z-axis, there are three moments of inertia of I_a , I_b , and I_c classifying the rigid rotors into four types: spherical (e.g., CH_4 ...), linear (e.g., CO_2 , C_2H_2 , HCl ...), symmetrical (e.g., NH_3 ...), and asymmetrical rotors (e.g., H_2O ...). Eq. (2.12) represents the rotational term $F(J)$ of the molecules that are linear ($I_b = I_c$, $I_a = 0$) and spherical ($I_a = I_b = I_c$) rigid rotors, which are the main focus of this thesis. For symmetrical ($I_{\parallel} \neq I_{\perp} = I_{\perp}$) model, $F(J)$ must be expanded with the second rotational quantum number K and the second rotational constant A , which is responsible for the parallel vibrational mode in addition to the rotational constant B for the perpendicular mode.

Needless to say, Eq. (2.12) is an ideal model and the moment of inertia of a real-life molecule varies under the effect of centrifugal distortion D . The molecular bond is not completely rigid, but it acts as a spring connecting two atoms. The nucleus tends to be expanded outwards (i.e., r increases due to stretching) by the centrifugal forces, decreasing rotational constant B for higher angular momentum:

$$F(J) = B \cdot J \cdot (J+1) - D \cdot J^2 \cdot (J+1)^2 \quad (2.13)$$

Nevertheless, the vibration-rotation transition $S(\nu, J)$ and its corresponding branches can be explained with the simplifying assumption that there is no anharmonic oscillation and the molecules are rigid rotors. In terms of wavenumber, $S(\nu, J)$ is expressed by combining the vibrational $G(\nu)$ and rotational $F(J)$ terms of that transition. Each transition line coming from distinctive vibrational and rotational energy levels contributes to the development of a specific vibration-rotation band (see Fig. 2.7 for CO_2).

$$S(v, J) = G(v) + F(J) = \bar{\nu} \cdot \left(v + \frac{1}{2} \right) + B \cdot J \cdot (J+1) \quad (2.14)$$

In the model of rigid rotors for linear molecules, the vibration-rotation transitions are allowed under the selection rule of $\Delta J = J' - J'' = \pm 1$, where the double prime denotes for lower energy level and higher level corresponds to single prime. Each value of ΔJ is classified into two main branches: P-branch which is responsible for all transitions that yield $\Delta J = -1$ and R-branch consists of all transitions that yield $\Delta J = +1$. The vibration-rotation observation between the two transitional levels is modified from Eq. (2.14) as:

$$S(v' \leftarrow v'', J' \leftarrow J'') = G(v') - G(v'') + B' \cdot J' \cdot (J'+1) - B'' \cdot J'' \cdot (J''+1) \quad (2.15)$$

The equation describing P- and R-branches can be simplified further. Having $J' = J'' - 1$ for P-branch and $J' = J'' + 1$ for R-branch from the selection rule, one can achieve Eq. (2.16) and Eq. (2.17) where ΔG_{vibrot} is shortened as $G(v') - G(v'')$:

$$S_P(v' \leftarrow v'', J' \leftarrow J'') = \Delta G_{\text{vibrot}} - (B' + B'') \cdot J'' + (B' - B'') \cdot J''^2 \quad (2.16)$$

$$S_R(v' \leftarrow v'', J' \leftarrow J'') = \Delta G_{\text{vibrot}} + 2B' + (3B' + B'') \cdot J'' + (B' - B'') \cdot J''^2 \quad (2.17)$$

Moreover, there is a possibility that ΔJ can equal zero, which is demonstrated by the existence of a Q-branch. However, these transitions are only possible when the orientation of the oscillating dipole moment is perpendicular relatively to the principal axis, which usually associates with vibrational bending motion for linear molecules and results in perpendicular bands. Eq. (2.18) describes all the transitions that yield $\Delta J = 0$ ($J' = J''$).

$$S_Q(v' \leftarrow v'', J' \leftarrow J'') = \Delta G_{\text{vibrot}} + (B' - B'') \cdot J'' + (B' - B'') \cdot J''^2 \quad (2.18)$$

The three observable branches coming from each vibration-rotation transitional level are graphically shown in Fig. 2.5.

In a given band, the intensity of a spectral line depends on the rotational population of the lower energy initial state (v', J'') and the state degeneracy. In the vibration-rotation spectrum, the intensity distribution among these transitions can be defined using the Boltzmann's population distribution:

$$\frac{N_{J''}}{N_0} = (2J'' + 1) \cdot \exp \left[- \frac{h \cdot c \cdot B'' \cdot J'' \cdot (J'' + 1)}{k_B \cdot T} \right] \quad (2.19)$$

Eq. (2.19) expresses that the strength of line intensities scales correspondingly with the population $N_{J''}$ of the molecular rotational states. In this equation, the term $(2J'' + 1)$ describes the degeneracy degrees of a linear molecule. The meaning of Eq. (2.19) is depicted in the bottom panel of Fig. 2.5. The transition starting from the centre line (i.e., starting from the small value of J) is dominated by the degeneracy of rotational states, causing its line intensities to linearly rise with increasing J . However, after reaching a certain limit of J at a larger value, the exponential factor given by the

thermal distribution then dominates and makes the population $\frac{N_j}{N_0}$ to decrease, causing the line intensities to drop accordingly.

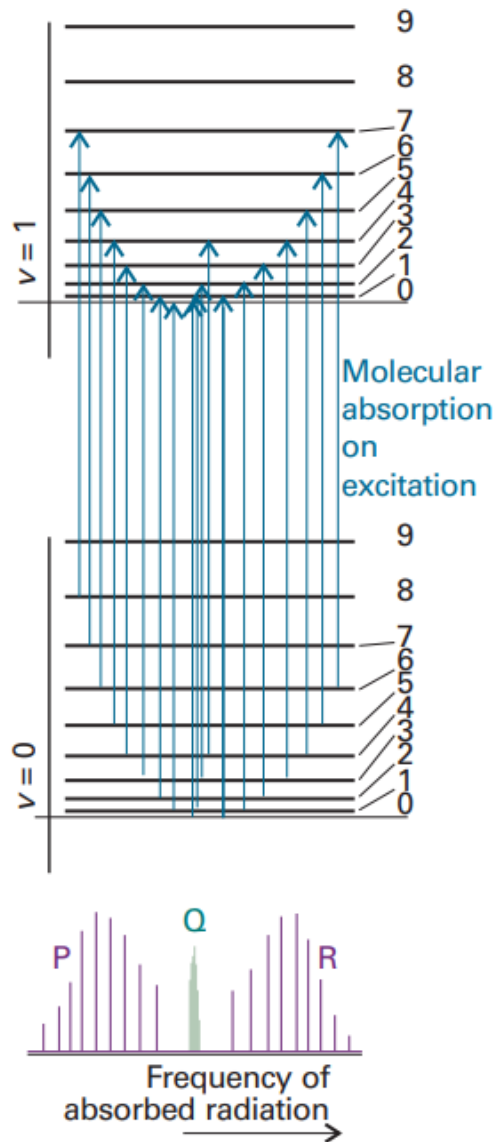


Figure 2.5. The schematic illustration of the molecular vibration-rotation spectral bands and their transitions are depicted accordingly. The P- and R-branches are responsible for all transitions that yield $\Delta J = -1$ and $\Delta J = +1$ respectively, while the Q-branch consists of all lines with $\Delta J = 0$ and do not appear in the case of parallel bands. The spectrum consists of all resulting branches and locates at a certain wavenumber range making up a specific “band” (Atkins & Paula, 2014).

2.2.3 CARBON DIOXIDE (CO₂)

Polyatomic molecules are grouped into linear and nonlinear molecules. The whole motion of a nonlinear molecule (e.g., H₂O...) is represented in terms of degrees of freedom $3N$ where N is the number of atoms of that molecule and is comprised of three degrees of rotational freedom, three degrees of translational freedom and the remaining degrees of freedom of $3N - 6$ are corresponding

to the vibrational movement of the molecule. In the case of linear molecules, such as CO_2 , they only possess two degrees of rotational freedom as there is no rotational moment of inertia around the internuclear axis, resulting in the degrees of vibrational freedom of $3N - 5$.

CO_2 has 3 atoms in total, including 1 atom of carbon and 2 atoms of oxygen, making its degrees of vibrational freedom to be $3N - 5 = 4$. It possesses four fundamental vibrational modes with a corresponding wavenumber depicted in Fig. 2.6. One acknowledges that the vibrational motion is related to the changes in bond length (e.g., stretching...) and bond angle (e.g., bending...), either in-plane or out-of-plane movements. The modes $\nu_1 = 1388 \text{ cm}^{-1}$ and $\nu_3 = 2349 \text{ cm}^{-1}$ are respectively the symmetric and asymmetric stretching motion of CO_2 , whereas the mode $\nu_2 = 667 \text{ cm}^{-1}$ corresponds to its bending movement. It is clear that the first mode ν_1 is infrared-inactive since there is no change in dipole moment. The three remaining modes are infrared-active, where $\nu_3 = 2349 \text{ cm}^{-1}$ results in parallel bands and yields no Q-branch, while both bending modes at $\nu_2 = 667 \text{ cm}^{-1}$ which degenerate twice is responsible for the observation of Q-branch in the vibration-rotation spectrum due to its perpendicular bending motion with respect to the principal axis.

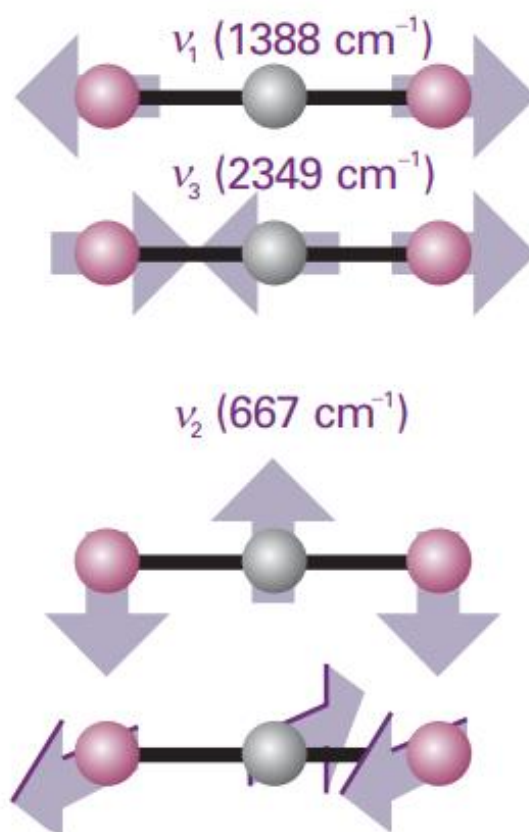


Figure 2.6. Illustration adapted from Atkins & Paula (2014) showing four normal vibration modes of CO_2 . Modes ν_1 and ν_3 are symmetric and asymmetric stretch, while mode ν_2 describes bending motion in-plane and out-of-plane.

Near-infrared bands of CO₂ can be due to either the overtone of vibrational modes or the dynamic combinations of its four normal modes. CO₂ was recorded to possess more than 500 bands with different intensity strengths throughout the infrared region at a distinctive centred wavelength. To describe a specific band of CO₂, one uses the notation ($\nu_1\nu_2\ell\nu_3r$), which is the superposition of ν_1 symmetric stretch, overtone ν_2 bending and overtone ν_3 asymmetric stretch. Angular momentum quantum number ℓ is associated with bending degenerated mode and r describes the ranking index of Fermi-resonance perturbation (Griffioen, 2021). In this study, the relevant CO₂ absorption band with the centred wavenumber at 4978 cm⁻¹ is used for the near-infrared open-path analysis with LINEFIT software. This band describes all transitions from the ground state to the higher states given by the (20012) superposition (i.e., denoting as 20012←00001). Fig. 2.7 below demonstrates the P- and R-branches of the band 20012←00001, which was plotted through the data given by the high-resolution transmission molecular absorption (HITRAN) 2020 Database¹. The HITRAN database is a compilation of spectroscopic parameters (e.g., line strength, temperature dependence, pressure broadened line half-width...) that were dedicatedly measured or numerically calculated for simulating and predicting the transmission spectra of atmospheric gases.

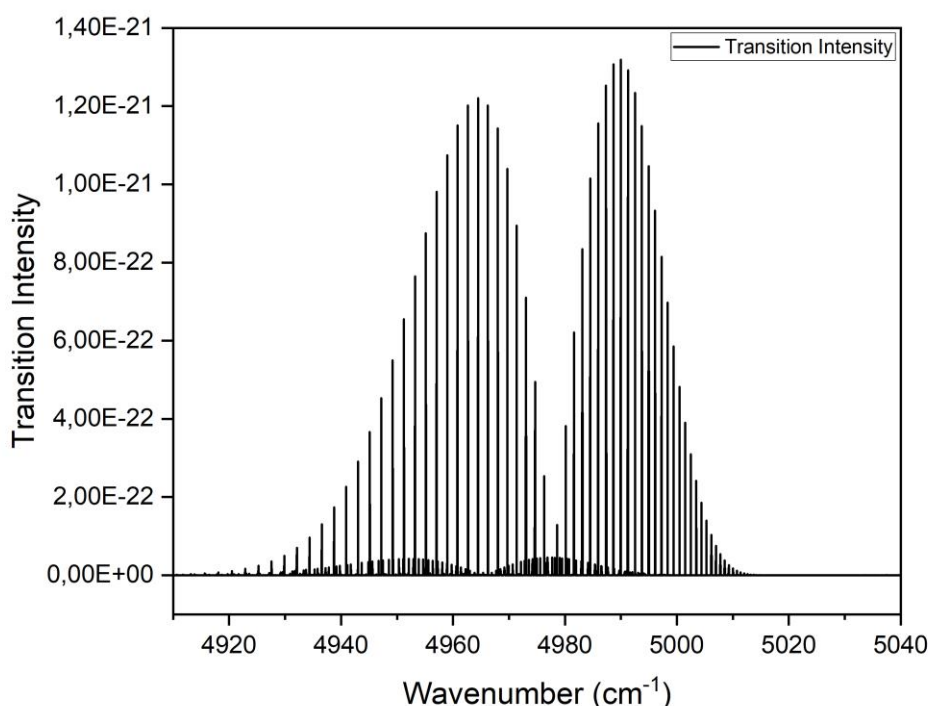


Figure 2.7. Simulated transition intensity of CO₂ (isotopologues was ¹²C¹⁶O₂) absorption band 20012←00001 centred at 4978 cm⁻¹. There is a small overlap with another band 21112←01101 at 4965.3851 cm⁻¹ which was included in the HITRAN database.

¹ <https://hitran.org/>

2.3 Molecular Intensity and Line Shape

Spectral lines are not infinitely narrow. Numerous physical factors attribute to this broadening, giving the line profile a specific shape and a finite linewidth. This section studies the spectral line intensity, which was consulted from Odintsova et al. (2017) and Okajima et al. (2006), and the two main contributors to the line broadening profile in remote-sensing application: Doppler and collision broadenings, which were mainly based on Hollas (2004) and Schrodin (2018).

2.3.1 THE INTENSITY OF SPECTRAL LINES

In the measurement of gas concentrations, the information from the detected radiation field on which the trace gas leaves its signature through absorption events can be retrieved based on Beer-Lamber's law. The transmitted intensity $I(\bar{\nu})$ at a specific wavelength is determined as:

$$\frac{I(\bar{\nu})}{I_0} = e^{-\alpha(\bar{\nu}) \cdot L} \quad (2.20)$$

Here, I_0 is the incident radiation intensity, L is the atmospheric absorption pathlength in cm and $\alpha(\bar{\nu})$ is the absorption coefficient in cm^{-1} , which is further defined by Eq. (2.21) for a given vibration-rotation transition of the target gas g :

$$\alpha(\bar{\nu}) = S(T) \cdot g(\bar{\nu} - \bar{\nu}_0) \cdot N_g \quad (2.21)$$

S is the line strength at a certain temperature T and is written in the unit of either $\frac{\text{cm}}{\text{molecule}}$ or $\frac{1}{\text{cm}^2 \cdot \text{atm}}$, $g(\bar{\nu} - \bar{\nu}_0)$ is the normalized line shape function in cm, N_g is the molecular number density ($\frac{\text{molecule}}{\text{cm}^3}$) of the target gas g and is equivalent to the product of the total sample gas pressure P in atm and its considered mole fraction X_g in that sample gas. The line shape function is governed by the temperature, pressure and mixture compositions through Doppler and collision broadenings. From Eq. (2.20) and (2.21), the absorbance for a given vibration-rotation transition can be integrated as:

$$A = - \int \ln \left[\frac{I(\bar{\nu})}{I_0} \right] d\bar{\nu} = S(T) \cdot N \cdot L \quad (2.22)$$

Eq. (2.22) is also directly proportional to the intensity of each line transition in an absorption band over a spectral range of wavenumber $\bar{\nu}$. Therefore, the band intensities of a gaseous molecule exponentially depend on the available number of molecules along the relevant path, as well as other sample-related factors (e.g., temperature, pressure...). In addition to the integrated absorbance, parameters such as pressure width and line centre frequency can also be retrieved by fitting the measured profile to a specific line shape model.

2.3.2 NATURAL LINEWIDTHS

Even if there is no physical external mechanism that could cause the broadening of the line profile, the width of the spectral line is still finite due to the finite lifetime τ of the excited state. As a direct

consequence of Heisenberg's uncertainty principle, a fundamental connection between lifetime uncertainty and energy uncertainty arises:

$$\Delta E \cdot \Delta t \gtrsim \frac{\hbar}{2} \quad (2.23)$$

The minimum width of the spectral line $\Delta\omega \gtrsim \frac{1}{2 \cdot \Delta t}$ can be derived from Eq. (2.23) based on its relationship with energy $\Delta E = \hbar \cdot \Delta\omega$ and $\hbar = \frac{h}{2\pi}$. This means that the spectral line is narrow for a long-lived excited state with lower energy uncertainty. Lifetime or natural broadening gives the line profile the Lorentzian shape, which can be illustrated by Eq. (2.24) and Fig. 2.8.

$$\frac{I(\omega)}{I_0} = \frac{\gamma}{2\pi \left[(\omega - \omega_0)^2 + \left(\frac{\gamma}{2}\right)^2 \right]} \quad (2.24)$$

Here, $\gamma = \frac{1}{\tau}$ is the full width at half maximum (FWHM) called natural linewidth and ω_0 is the centre frequency. However, in remote-sensing application, the natural broadening is usually neglected as the resulting linewidth is dominated by external physical influences, such as Doppler and pressure broadening.

2.3.3 COLLISION BROADENING

Collision or pressure broadening affects the line profile when the thermal motion collision between molecules or atoms occurs. This process shortens the lifetime of an excited state and causes the spectral line to be broader. In a high-pressure environment where the molecular number density is large, the probability for homogeneous collision broadening to occur is higher than in a low-pressure condition (i.e., high-altitude atmospheric layer). Therefore, this broadening effect is the dominator in the troposphere layer. Similar to natural broadening, the line profile of collision broadening follows the Lorentzian distribution as shown in Eq. (2.25). Considering τ_C to be the mean time between collision, the FWHM $\delta\omega_C$ of this Lorentzian profile is:

$$\delta\omega_C = \frac{1}{2\pi\tau_C} \quad (2.25)$$

2.3.4 DOPPLER BROADENING

As the name recalls, the Doppler broadening of the spectral line comes from the Doppler effect, which considers the motions of atoms or molecules with velocity v as an emitting or absorbing source under different observer's perspectives. In case of the greenhouse effect where GHGs thermally emit radiation, this broadening is referred to as thermal Doppler broadening. In an equilibrium gaseous system with finite temperature $T > 0$ °K, the statistical velocity distribution of the emitting particles with mass m is defined by Maxwell-Boltzmann distribution:

$$P_{\nu} \cdot d\nu = \sqrt{\frac{m}{2\pi \cdot k_B \cdot T}} \cdot e\left(-\frac{E_{kin}}{k_B \cdot T}\right) \cdot d\nu \propto e\left(-\frac{m \cdot \nu^2}{2 \cdot k_B \cdot T}\right) \quad (2.26)$$

Here, E_{kin} is the kinetic energy and relates to velocity as $E_{kin} = \frac{1}{2} \cdot m \cdot \nu^2$. Due to the influence of the Doppler effect, the frequency of the incident radiation is shifted by:

$$\omega = \omega_0 \left(1 - \frac{\nu}{c}\right) \quad (2.27)$$

By inserting the relation of Eq. (2.27) into Eq. (2.26), the distribution is re-written in the form of frequency as:

$$P_{\omega} \cdot d\omega \propto e^{-\left[\frac{(\omega - \omega_0)}{\omega_0 \cdot \nu_p} \cdot c\right]^2} \cdot d\omega \quad (2.28)$$

Here, the probable velocity is defined as $\nu = \sqrt{\frac{2 \cdot k_B \cdot T}{m}}$ derived from Eq. (2.26). Eq. (2.28) shows that the line profile of Doppler broadening follows Gaussian distribution:

$$\frac{I(\omega)}{I_0} = e^{-\left[\frac{(\omega - \omega_0)}{\omega_0 \cdot \nu_p} \cdot c\right]^2} = e^{-\left[\frac{(\omega - \omega_0)}{\delta\omega_D} \cdot \sqrt{4 \cdot \ln(2)}\right]^2} \quad (2.29)$$

Where the FWHM $\delta\omega_D$ of Gaussian profile is:

$$\delta\omega_D = \frac{\omega_0}{c} \cdot \sqrt{\frac{8 \cdot k_B \cdot T \cdot \ln(2)}{m}} \quad (2.30)$$

It should be noted that Eq. (2.30) and Eq. (2.29) are only valid when other broadening contributors are considerably small. Doppler broadening dominates in the upper atmosphere as the pressure steadily decreases. In remote-sensing application, since both pressure and Doppler broadenings contribute equivalently to the broadening of the line profile of a gas molecule, the resulting spectral line is approximated by a Voigt profile, which is the convolution of Gaussian and Lorentzian shape.

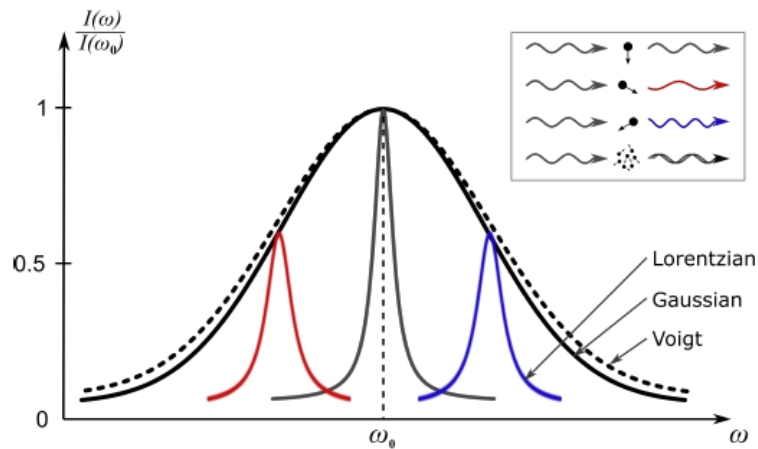


Figure 2.8. Demonstration of collision (Lorentzian) and Doppler (Gaussian) broadenings. Lorentzian profile (red, grey, and blue) represents frequency shifts due to different motions of emitting molecules (Schrodin 2018).

2.4 Fourier Transform Infrared spectroscopy

In comparison to the first commercially available IR spectrometer in the 1940s, the introduction of the Fourier-Transform concept into this application at the later stage has drastically enhanced the initial quality of infrared spectra and reduced the measurement time. Along with the continuously improving computer technology, the Fourier Transform spectrometer (FTS) has been greatly contributing to various branches of spectroscopic research and is specifically ideal for the optical remote-sensing application, where the concentration of the infrared-active trace gases in the Earth's atmosphere can be daily and frequently monitored. FTIR spectrometers can be also operated on different flexible platforms (e.g., mounted on aircraft, balloon, satellite...) for the study of atmospheric trace gases.

This section is mainly consulted from the textbooks of Eismann (2012), Siesler et al. (2001) and Stuart (2004). Moreover, important aspects such as the instrumental line shape (ILS) and the LINEFIT program are also based on the research articles of Hase et al. (1999) and Frey et al. (2015).

2.4.1 CONCEPT OF FOURIER TRANSFORMATION

FTIR spectroscopy aims to obtain spectral interferograms, which is induced by the superposition of two beams from the same electromagnetic source over a range of optical path. Based on these resulting interferograms, the desirable information about the spectrum of the source is derived with the use of a well-established mathematical Fourier transform. The Michelson interferometer is a well-known realization that is commonly utilized in FTIR architecture. As shown in Fig. 2.9, the interferometer consists of two mirrors, where one is fixed and the other one is allowed to move at a certain distance d , and a beam splitter (BS) which splits the incident light beam from the radiation source (e.g., Sun, broadband light source, atmospheric emission...) into equal portions. Here, 50 % of the incident light is directed perpendicularly to the fixed mirror, while 50 % is transmitted directly through the beam splitter and reflected by the movable mirror. Two then reflected beams from the two mirrors are recombined by the BS and interfere at the same position, where again half of the recombined modulated light containing the information on the interference patterns propagates through the BS and is detected by the detector (i.e., transmitted beam), and its other half is reflected back to the incoming direction of the radiation source. From the description, the relationship between the total transmission τ_1 of one arm and the other arm τ_2 should be $\tau_1 = \tau_2 = \frac{1}{2}$, but this is an ideal theoretical assumption and the BS deviates from a 50:50 splitting ratio in real-life scenarios. A compensator having the same thickness as the BS is added to eliminate the dispersion effect given by the BS material. Furthermore, an additional reference interferometer using an artificial source of either white light or laser is usually placed within the FTS interior to determine the position of the moving mirror. As it is extremely crucial to accurately control the

optical path difference (OPD) between the interfering paths, the EM27/SUN spectrometer is equipped with Helium-Neon (HeNe) laser to complete the task (see Fig. 3.1).

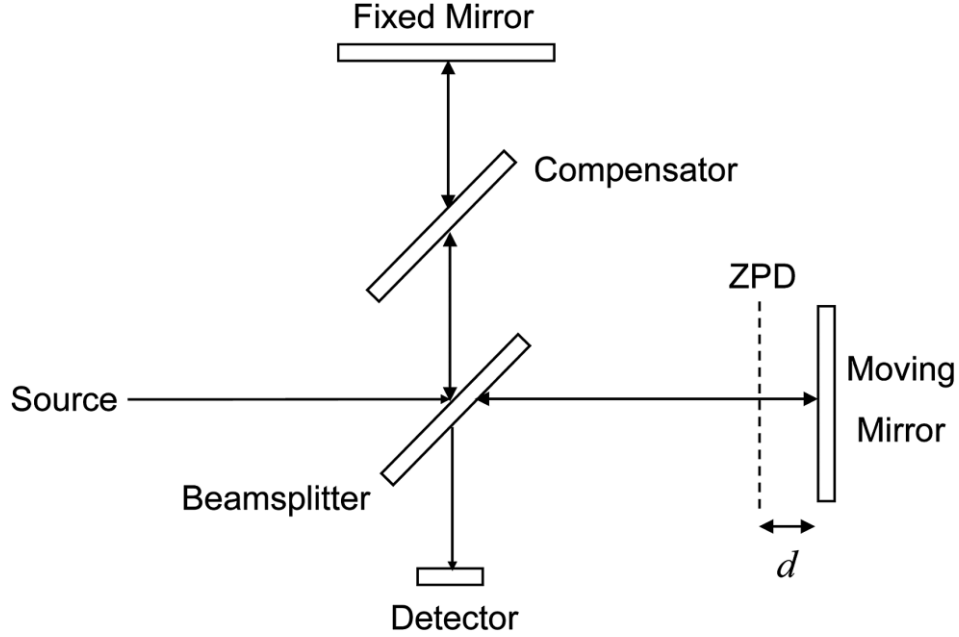


Figure 2.9. Schematic sketch of the standard Michelson interferometer. OPD between the interfering wavefronts is zero when the movable mirror reaches the zero-path difference (ZPD) positions (Eismann, 2012).

In interferometry, the total intensity given by the superposition between two plane waves can simply be calculated by the summation of each wave vector. Considering two monochromatic plane waves with complex amplitudes (i.e., $E_1 = \sqrt{\tau_1 E_0} \cos(\omega t - kz)$ and $E_2 = \sqrt{\tau_2 E_0} \cos[\omega t - k(z + \Delta)]$, $k = \frac{2\pi}{\lambda}$ is the angular wavenumber, $\omega = 2\pi\nu$ is the angular frequency), where each propagates in the z direction and has the same intensity E_0 , but assuming that there is a delay in OPD between them at a distance $\Delta = \frac{2d}{\cos\theta}$ (i.e., θ is the incident angle between the optical axis and incoming plane wave and d is the displacement from the ZPD), their superposition in an ideal case $\tau_1 = \tau_2 = \frac{1}{2}$ is

$$\begin{aligned}
 E(\Delta) &= |E_1 + E_2|^2 \\
 &= |E_1|^2 + |E_2|^2 + E_1^* E_2 + E_1 E_2^* \\
 &= \frac{1}{2} E_0 \cos[1 + \cos(2\pi\nu\Delta)]
 \end{aligned} \tag{2.31}$$

Eq. (2.30) is understood as the interference equation, where $\phi = 2\pi\nu\Delta$ is the result of the phase summation between two waves. The final interference intensity depends on the OPD introduced by the movable mirror at a certain position, leading to constructive and destructive interference. A constructive pattern is observed when OPD is an even integer multiple of λ , while an odd OPD integer multiple of $\frac{\lambda}{2}$ gives destructive interference.

In real-life scenarios, the radiation source gives off light that is non-stationary polychromatic with the spectral intensity of $E_0(\bar{\nu})$, not a perfect stationary monochromatic field as theoretically depicted (see the difference in Fig. 2.10). Interference equation of polychromatic source can be derived by integrating Eq. (2.31) over all the considering wavenumbers:

$$E(\Delta) = \int_{-\infty}^{+\infty} \frac{1}{2} E_0(\bar{\nu}) [1 + \cos(2\pi\bar{\nu}\Delta)] d\bar{\nu} \quad (2.32)$$

$$= \int_{-\infty}^{+\infty} \frac{1}{2} E_0(\bar{\nu}) d\bar{\nu} + \int_{-\infty}^{+\infty} \frac{1}{2} E_0(\bar{\nu}) \cos(2\pi\bar{\nu}\Delta) d\bar{\nu}$$

The first term of Eq. (2.32) denoted as $E_{DC}(\Delta)$ represents the constant part, while the second term denoted as $E_{AC}(\Delta)$ describes the modulated fluctuating part of the FTS. The right-hand side polychromatic illustration in Fig. 2.10 is understood as a two-sided interferogram, caused by the mirror-symmetrical movement around its centre ZPD position (i.e., OPD = 0). In practical cases, the bias term $E_{DC}(\Delta)$ is usually removed by using an electronic AC-coupled detector. The EM27/SUN spectrometer, however, records DC-coupled interferograms, as this allows to remove the effects of source brightness fluctuations during the subsequent processing. $E_{AC}(\Delta)$ is treated as the real-value interferogram and contains all spectral information of radiation falling onto the detector. From now on, the interferogram symbol $E_{AC}(\Delta)$ will be referred as $E(\Delta)$ instead.

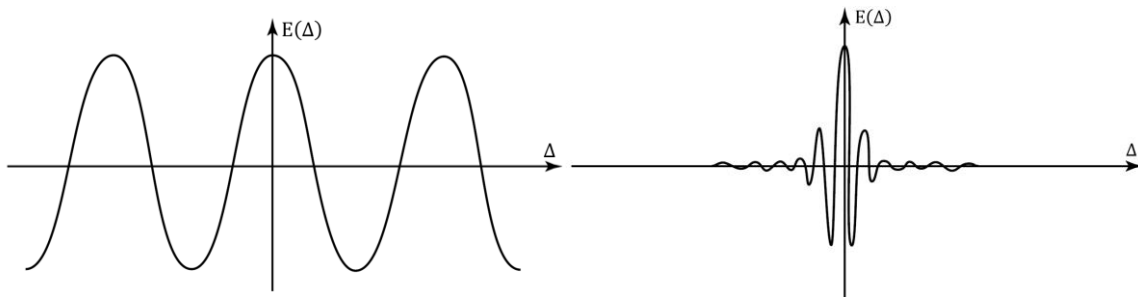


Figure 2.10. Interferograms of monochromatic versus polychromatic source, modified and adapted from Stuart (2004).

2.4.2 FOURIER TRANSFORM MATHEMATICS

Having the information of the interferogram $E(\Delta)$ from Eq. (2.32), the source spectrum $S(\bar{\nu})$ can be achieved through the link given by the Fourier transformation:

$$E(\Delta) = \int_{-\infty}^{+\infty} S(\bar{\nu}) \exp(-i2\pi\bar{\nu}\Delta) d\bar{\nu} \quad (2.33)$$

$$S(\bar{\nu}) = \int_{-\infty}^{+\infty} E(\Delta) \exp(i2\pi\bar{\nu}\Delta) d\Delta \quad (2.34)$$

In practice, the measured interferogram is sampled equally and uniformly with discrete spaced N points, not continuous shown in the equations above. Eq. (2.34) must be re-defined as:

$$S(\bar{\nu}) = \frac{1}{N} \sum_{j=1}^N E(\Delta_j) \exp(i2\pi\bar{\nu}\Delta_j) \quad (2.35)$$

In Eq. (2.35), $\Delta_j = j \cdot \delta$ depicted here is the OPD respectively corresponding to each interferogram N point. Considering that the mirror displacement between each N sample is δ , one must obey the Nyquist sampling theorem stated in Eq. (2.36), where δ must be properly chosen to obtain a meaningful interferogram for a given spectral bandwidth.

$$2\bar{\nu}_{\max} = \frac{1}{2\delta} \quad (2.36)$$

Eq. (2.36) states the required condition for a continuous signal to be reconstructed from the discrete sampling spectrum. The wavenumber corresponds to the wavelength $\lambda_{\min} = 4\delta$. If this criterion is not satisfied, one would observe the aliasing effect, which is a systematic distortion and is contributed by the folding of spectra with a frequency larger than the allowed maximum Nyquist value. For this reason, the He-Ne laser of the EM27/SUN spectrometer (i.e., $\lambda_{\text{He-Ne}} = 633 \text{ nm}$) is utilized to control δ by sampling the interferogram at each zero crossing of the laser AC interferograms. In other words, the interval δ is defined by these zero crossings.

2.4.3 COMPUTATION OF FTS SPECTRAL FEATURES

2.4.3.1 Apodization function

Eq. (2.34) assumes the mirror moves at an infinite distance integrating from $+\infty$ to $-\infty$, which is physically impossible in reality. In fact, the maximum OPD retardation, named L_{\max} , is restricted depending on the limit of the mirror's symmetrical displacement d around its ZPD centre, leading to the observation of a truncated interferogram. Considering that a realistic OPD range of the mirror is from $-L_{\min}$ to L_{\max} , one recognizes that the truncated interferogram $E_{\text{finite}}(\Delta)$ is mathematically defined as the product of its infinite ideal interferogram $E_{\text{infinite}}(\Delta)$ with a boxcar function $U(\Delta) = 1$ if $\Delta \leq |L_{\max}|$, otherwise $U(\Delta) = 0$ with $\Delta > |L_{\max}|$ which describes the mirror's finite movement (see the illustration in Fig. 2.11(a1)):

$$\begin{aligned} S_{\text{meas}}(\bar{\nu}) &= \int_{-L_{\max}}^{L_{\max}} E_{\text{finite}}(\Delta) \cdot \cos(i2\pi\bar{\nu}\Delta) d\Delta \\ &= \int_{-\infty}^{+\infty} E_{\text{infinite}}(\Delta) \cdot U(\Delta) \cdot \cos(i2\pi\bar{\nu}\Delta) d\Delta \\ &= F\{E_{\text{infinite}}(\Delta)\} \otimes F\{U(\Delta)\} \\ &= S_{\text{infinite}}(\bar{\nu}) \otimes [2L_{\max} \cdot \text{sinc}(2\pi\bar{\nu}L_{\max})] \end{aligned} \quad (2.37)$$

As derived in Eq. (2.37), the actual measured vibration-rotation finite spectrum $S_{\text{meas}}(\bar{\nu})$ is defined as the convolution of the Fourier transform of an ideal interferogram $E_{\text{infinite}}(\Delta)$ which is equivalent to $S_{\text{infinite}}(\bar{\nu})$ and $2L_{\max} \cdot \text{sinc}(2\pi\bar{\nu}L_{\max})$ corresponding to the Fourier transform of $U(\Delta)$. Note that the same $S_{\text{meas}}(\bar{\nu})$ can be obtained with the use of cosine transform, as Eq. (2.34) results in the real-

value due to the symmetry of the interferogram. $F\{U(\Delta)\}$ is referred as the instrumental line shape (ILS) function (see Fig. 2.11(a2)), which is defined as the instrument response to an ideal monochromatic spectral line (Davis et al., 2001). Its spectral resolution $\Delta\bar{\nu}$ is equivalent to the FWHM of $\frac{0.6}{L_{\max}}$. Moreover, it is also important to note that the ILS of an ideal FTS given in this figure does not represent the true ILS spectral response function of a real-life FTS. This deviation will be mentioned more clearly in the next subdivision.

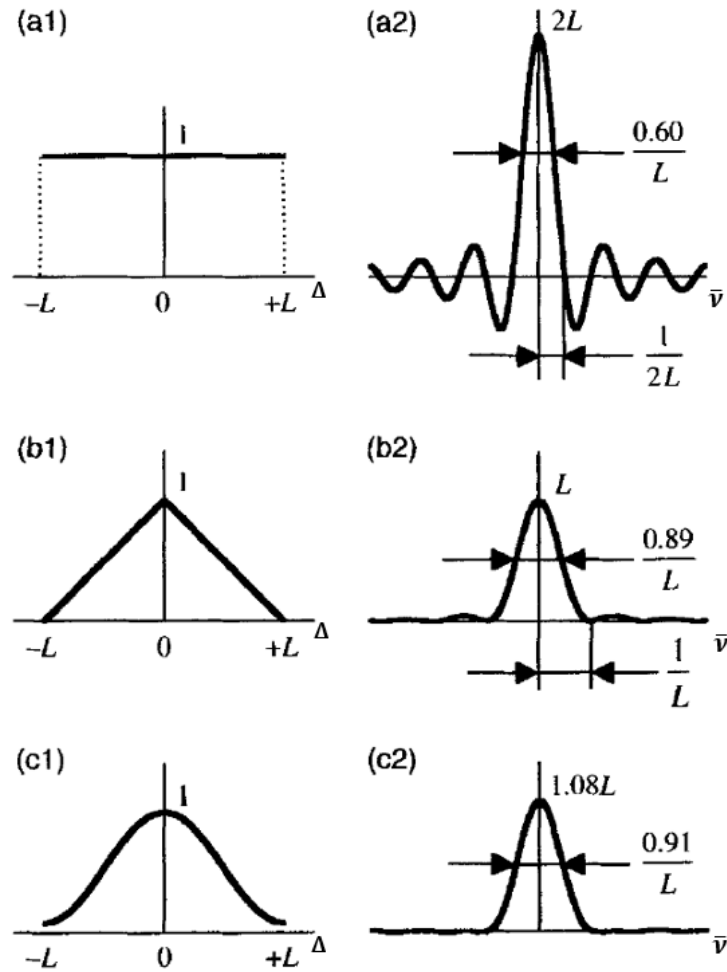


Figure 2.11. The figure adapted and modified from Siesler et al. (2002) represents the apodization model of boxcar (a1), triangular (b1) and Happ-Genzel (c1) functions. (a2), (b2) and (c2) are the corresponding ILS functions respective to the used apodization model.

The spectral purity of the instrument is limited due to the induced negative side lobes from the sinc function, but their amplitude can be suppressed by multiplying the interferogram or the boxcar function with a weighting function, resulting in a broader FWHM and lower amplitude. This modification is known as apodization in the context of computational discrete Fourier transform, which applies either triangle or Gaussian functions (see Fig. 2.11). Nevertheless, there is a trade-off between spectral purity and spectral resolution if apodization is used. One notices that the resolution with cosine apodization in Fig. 2.12 is slightly not as good as without the function.

Contrarily, the misinterpretation of the spectral features can be prevented with apodization. For the EM27/SUN spectrometer, a sufficient compromise between resolution and the side-lobe suppression can be achieved by utilizing the Norton-Beer medium apodization function, defining the resolution as $\Delta\bar{\nu} = \frac{0.9}{L_{\max}}$.

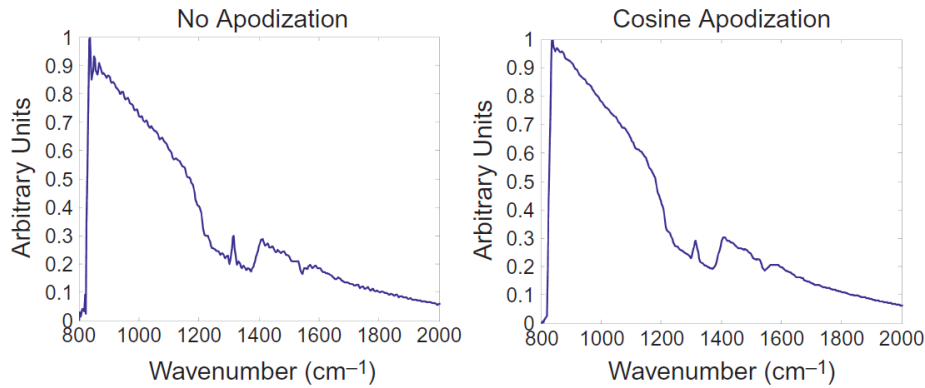


Figure 2.12. Example of reconstruction spectra of CH₄ modified and adapted from Eismann (2012), where the left-hand and right-hand sides are without and with apodization.

2.4.3.2 Instrumental line shape (ILS)

In the remote sensing application of FTS, numerous factors can impede a precise retrieval of the trace gas profile in the atmosphere. That is to say, a state-of-the-art retrieval algorithm software usually requires three main models to accurately fit those factors: the atmospheric radiation transfer model, the instrumental model of ILS and the inversion algorithm. An accurate characterization of the ILS is an important task during the spectral analysis, otherwise, if one assumes the actual ILS is perfect and does not determine it properly, the systematic errors caused by the given incorrect ILS will propagate into the retrieved gas amount. The systematic deviation of the ILS is a result of two main faults: the first is modulation loss which happens for all FTS, including the ideal spectrometer through the inherent self-apodization of the instrument, and the second is due to the non-calibration, misalignment, error of electronic components and optical aberrations, which can be characterized by modulation efficiency (ME) amplitude and phase error (PE).

The self-apodization takes place because the interferometer accepts a finite field of view (FOV). The deviation from the parallel beam and the finite acceptance cone of incoming radiation alter the shape of ILS, which can be determined via the maximum OPD and the FOV of the EM27/SUN spectrometer. Moreover, while retrieving gas concentration from the spectra, the internal components of the spectrometer should be well-aligned such that the second contribution characterized by ME and PE as a function of OPD dependence can be minimized as much as possible. Both parameters can be determined from the dedicated open-path measurements by analysing either the observed shape of H₂O lines (Frey et al., 2015) or the gas-cell measurements

(Alberti et al., 2022). Fig. 2.13 illustrates both factors influencing the ILS, where the decrease of ME from its ideal value of 1.0 broadens symmetrically the amplitude and width of ILS shape, and the non-zero PE indicates its asymmetric change.

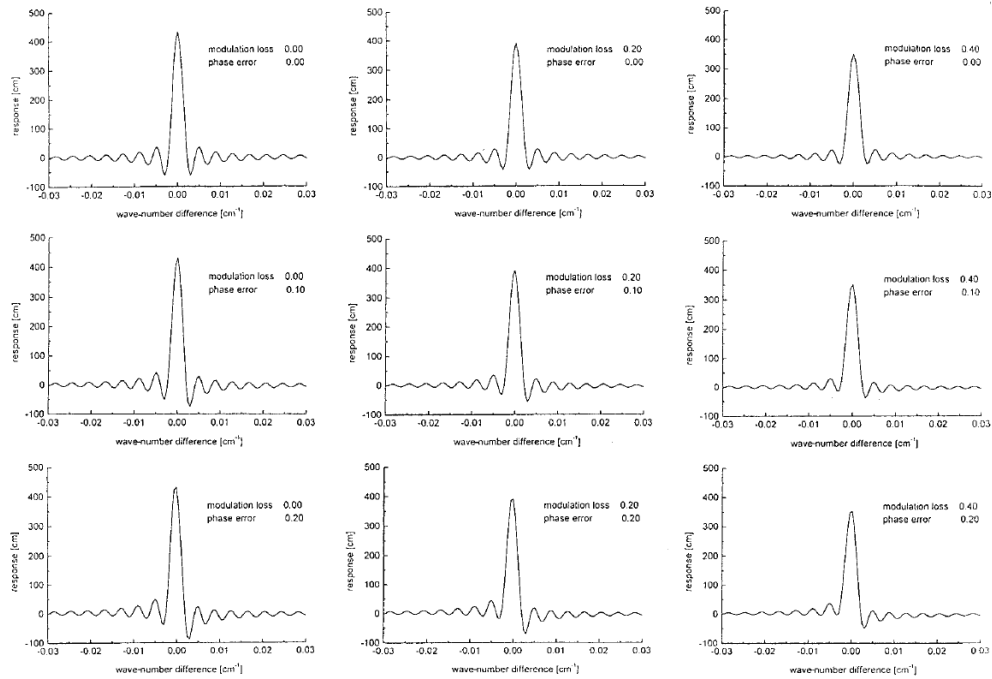


Figure 2.13. The demonstration adapted from Hase et al. (1999) shows two main factors used for describing the deviation of the actual ILS from its ideal shape. The ILS amplitude is broadened when the ME is smaller than 1 and is narrowed when the ME is larger than 1. The value 0 of the PE represents the symmetry of the ILS shape and a PE value that is larger than 0 would result in ILS asymmetry.

3 Instrument and Data Analytical Method

3.1 Fourier Transform Infrared EM27/SUN FTIR Spectrometer

A full description of the development of the EM27/SUN spectrometer, its components (e.g., home-built Camtracker) and its upgrades over the past few years has already been discussed in several journal articles and PhD research published by the IMK-ASF at KIT (Gisi et al., 2011; Gisi et al., 2012; Frey et al. 2015; Hase et al., 2016; Frey, 2018). In this section, a summary of the current EM27/SUN setup is provided.

The internal configuration of the EM27/SUN spectrometer is illustrated in Fig. 3.1, where the main optical components and the path that light propagates are depicted. As the light rays enter the spectrometer through the mirror arrangement of the solar tracker, it first meets the entrance window with a long-pass filter, blocking the undesired wavelengths range below 750 nm. The beams then propagate to Bruker's RockSolid™ pendulum interferometer, which composes of a pair of cube corner retroreflectors and a central BS of CaF₂. Since the pendulum mechanism carrying the two mirrors relies on a steel spring, the frictionless and wear-free motions of the scanner are achieved. This allows EM27/SUN to gain high thermal and mechanical stability, as well as to obtain better reliability than the IFS125HR of TCCON. Fig. 3.1 shows a top view of the opened EM27/SUN spectrometer. The resolution of 0.5 cm⁻¹ of the spectrometer corresponds to the maximum OPD of 1.8 cm. The HeNe laser in the middle of Fig. 3.1 is used for defining the interferogram's sampling intervals.

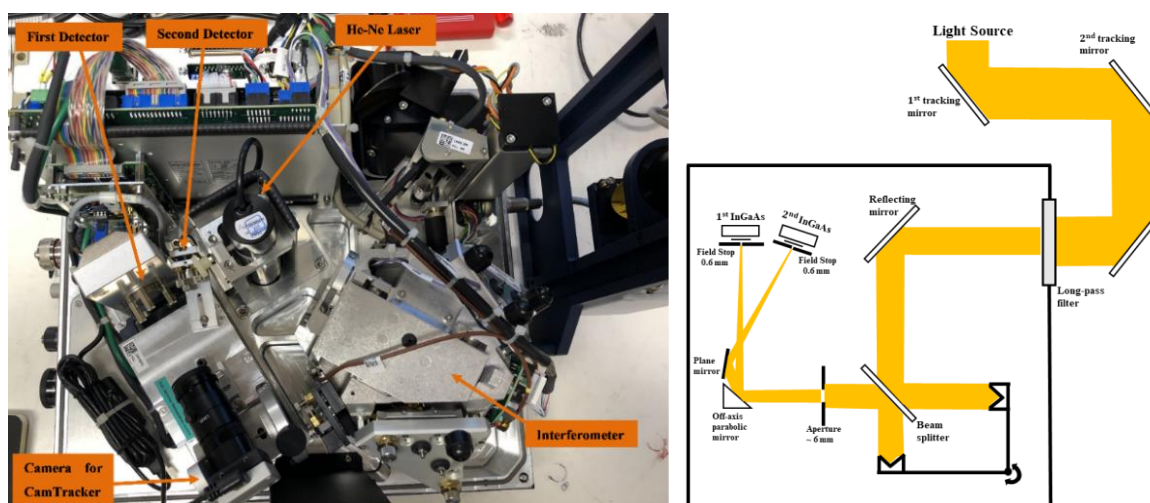


Figure 3.1. The left panel is the top view of the current EM27/SUN spectrometer. The right panel depicts the schematic drawing of the light propagation path coming from the polychromatic source and entering the spectrometer through its housing entrance.

After being modulated by the interferogram, the radiation is blocked by an aperture stop with a diameter of ~ 6 mm to control the optical aberrations and to prevent the nonlinear response of the detector. The beam is then focused by a 90° off-axis paraboloid mirror with a focal length of 127 mm onto the primary field stop with 0.6 mm in diameter. The corresponding semi-FOV is 2.36 mrad, which is equivalent to about half of the mean solar disk diameter ($\sim 0.135^\circ$). A DC-coupled InGaAs covering the spectral range from 5000 cm^{-1} to 12000 cm^{-1} records the interferograms, where the bands of CO_2 , CH_4 , O_2 and H_2O can be observable. Moreover, a second spectral channel was implemented by Hase et al. (2016). A second plane mirror integrated directly behind the parabolic mirror focuses the decoupling part of modulated light onto the corresponding field stop with 0.6 mm in diameter. This creates an intersection angle of roughly 25° between the reflected decoupling light and its primary beam. The additional detector placed after the second field stop is a windowless extended InGaAs diode, which expands the coverage range to the 4000 cm^{-1} region and enables the detection of CO , N_2O and water's deuterated isotopologue (HDO) bands. To avoid measuring the overlapping spectral range with the primary detector, a wedged Germanium long-pass filter is integrated between the additional diode and the second field stop. It is also important to note that a straightforward approach of directly replacing the primary detector to extend the spectral range is possible, but not preferable. This action would not only increase the spectrum's noise level, but also cause the retrieval data to be unreliable as the final gas profile of CO_2 was shown to be dependent on the overall signal level (Hedelius et al., 2016; Hase et al., 2016).

3.2 Light Source and Path-Extension Strategy

In open-path application, the study of CO_2 concentration in the near-infrared region requires the use of a conventional, high-temperature and high-brightness broadband light source. In this thesis, a simple light bulb of low-voltage Osram tungsten-halogen lamp 64602 (50W, 12V) was applied as the main light source. As the aim is to measure the target gas in a distance on the order of tens to hundreds of meters, the Halogen light bulb was integrated into a searchlight unit of a military leopard tank¹ (see Fig. 4.1), which is composed of an off-axis parabolic mirror (see Fig. 3.2) with an area of 78400 mm^2 and an effective focal length of 170 mm. By placing the source directly at the focal point of the mirror, the searchlight unit is able to achieve the ideal light collimation and support the beam size of 280 mm in horizontal and 280 mm in vertical directions. Given the filament area of 9 mm^2 , the solid angle of the light source is calculated to be $3.1 \cdot 10^{-4}$ steradians at 170 mm focal length, assuming its horizontal and vertical FOVs onto the mirror are roughly 0.02° and 0.02° .

¹ More information and pictures of the light source unit (e.g., dimensions, internal optical components...) can be found at http://www.hosin.de/Licht/Zielscheinwerfer_BSW/zielscheinwerfer_bsw.html



Figure 3.2. The Left and right figures demonstrate the internal structure on both sides of the source unit.

The field stop is an important component as it governs the FOV of the interferometer. To precisely control the spectrometer's line of sight (LOS), the light source is imaged onto the centre of the field stop's circular entrance by pointing the interferometer's FOV to the centre of the light source. As an example, when the Sun is applied as a light source, Gisi et al., (2012) illustrated how the solar disk's image can be viewed onto the field stop under two different FOV perspectives.

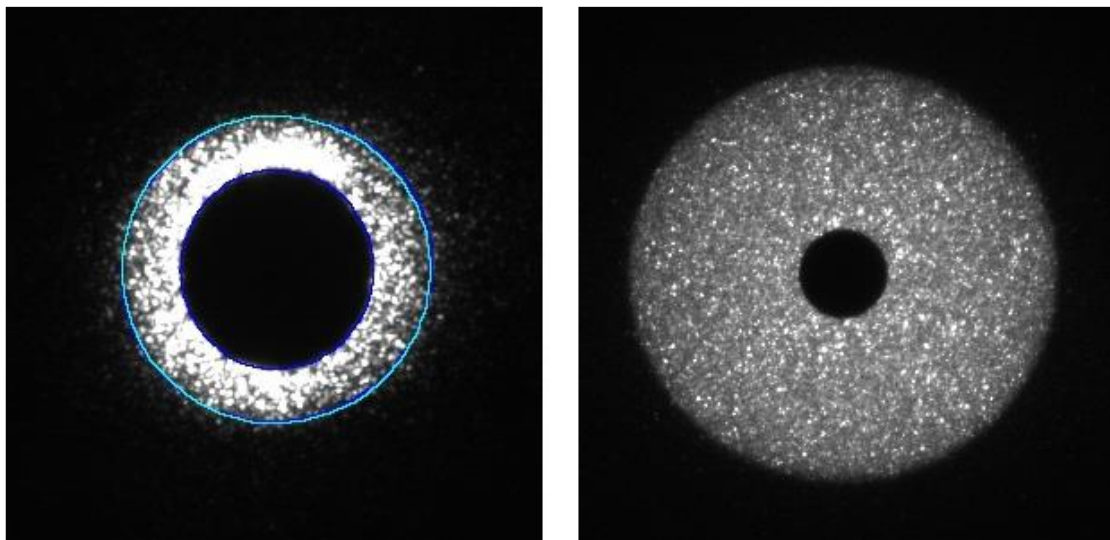


Figure 3.3. Adapted from Gisi et al., (2012), this figure demonstrates the solar disk's image onto the field stop of EM27/SUN (left panel, larger field stop, narrower FOV) and by IFS125HR (right panel, smaller field stop, wider FOV) spectrometers. The blue circles are applied by CamTracker to maintain tracking precision.

To obtain the highest possible signal level realized by a given source, the image of the light source formed by the spectrometer should be large enough to illuminate fully and homogeneously the diameter of the input field stop (i.e., the black circle at the centre in Fig. 3.3). This is equivalent to the requirement that any permitted ray leaving the spectrometer through the field stop is collected by the lamp and focused on the filament area. The condition is experimentally illustrated in Fig. 3.4 and is mathematically derived by Eq. (3.1).

$$B = g \cdot 2 \cdot \tan(\alpha') \quad (3.1)$$

α' is the angle that diverges outward from the spectrometer's aperture of 6 mm and approximately equals to the spectrometer's semi FOV of 0.135° , g is the estimated distance from the spectrometer's housing entrance to the applied light source, B is the total size of the source's image and represents the acceptance range that the spectrometer can detect within its FOV. Under a specific pathlength, Eq. (3.1) states the required size that the image should have in order to achieve a completed illumination on the spectrometer's acceptance FOV. For the spectrometer to capture all incoming light rays that only originate from the source, the open-path beam size must be larger or equal to the size of the formed image (i.e., $B \leq G$) under the chosen distance g .

For the atmospheric greenhouse retrievals, it is desired to perform the measurement on the order of km pathlength to detect the trace gases with small mixing ratios, such as XCH_4 (i.e., hundreds of meters to 20 km reported by Merten et al. (2011)). This implementation addresses the disadvantage of using the manmade light source in this case. When the Sun is used as the main source for trace gas measurements, there is no problem in imaging its solar disk onto the system's field stop over an extremely long distance as the apparent diameter of the solar disc is 0.5° . The Sun has a diameter of roughly 1390000 km, meaning that the maximum distance for the spectrometer to detect all incoming Sun rays within its acceptance cone is ~ 296 million km. This is nearly double the distance from the Earth to the Sun. A searchlight of 280 mm diameter offers an apparent diameter of 0.5° in just a distance of 32 m.

The realization of long-distance measurements is restricted by the beam size of the current open-path setup. This effect can be mathematically illustrated by Eq. (3.2), where the dimension of the source's image is connected by the equations of linear, longitudinal, and angular magnification of an optical system. Since the EM27/SUN spectrometer has a fixed magnification of 1x (i.e., $B = G$), the beam size G supported by the light source unit must be kept increasing until the optical system compensates the desirable km distance g , which is impractical in real-life setup. For the thesis's optical setup with a minimum of 0.27° apparent diameter, if one additionally accounts for the 6 mm aperture size (i.e., $B \leq G = 274$ mm), the maximum measurable pathlength that the spectrometer allows is ~ 58.14 m. Adding the distance from the spectrometer's housing entrance to the first tracking mirror (i.e., 33 cm), the actual allowed pathlength is 57.81 m. Without any further

improvements to the current setup, implementing the open-path measurements at a longer distance than 57.81 m would only introduce a considerable amount of noise to the recorded spectra.

$$M = \frac{B}{G} = \frac{b}{g} = \frac{\theta_{\text{exit}}}{\theta_{\text{entrance}}} \quad (3.2)$$

Here, b is the estimated distance from the source's image formed on the detector to the spectrometer's housing entrance. θ_{entrance} and θ_{exit} respectively denotes the angular size of the source and its image from the light propagating into and out of the optical system.

For astronomical observation, an optical telescope system composed of a set of lenses and mirrors is used to obtain an enlarged image of distant, faint, astronomical objects. In analogy, the image of a small faint light source can be enlarged by enhancing the overall magnification of the spectrometer with a telescopic system (see Eq. (3.2)). Furthermore, increasing the size of the light source by expanding the area of the mirror would improve the overall quality as well, but such a lamp source would soon reach impracticable dimensions. The insertion of a telescope allows one to realize longer path lengths, as well as to observe the weak near-infrared CO₂ bands.

Telescopes can be classified as reflectors (i.e., using mirrors) or refractors (i.e., using lenses). Light coming from a distant object is first imaged by the objective lens or primary mirror at the first focal point. The larger the diameter of the telescope's opening, the better the light gathering and resolving power. The intermediate image is then magnified by the ocular lens or secondary mirrors of the telescope and is recorded by the spectrometer. The magnified image of the source can then illuminate the full field stop at a longer distance. The telescope's magnification equation can be derived based on the corresponding trigonometrical calculation:

$$M = \frac{f_{\text{obj}}}{f_{\text{ocu}}} \quad (3.3)$$

Here, f_{obj} and f_{ocu} are the focal length of the objective and ocular lenses. Eq. (3.3) is based on the assumption that $\tan(\theta_{\text{entrance}}) \approx \theta_{\text{entrance}} = \frac{B'}{f_{\text{obj}}}$ and $\tan(\theta_{\text{exit}}) \approx \theta_{\text{exit}} = \frac{B'}{f_{\text{ocu}}}$ as the angular size is a small angle. B' is the intermediate image size of the source. In this thesis, an additional telescope system was also integrated into the measurement setup to enable a longer pathlength measurement, described in detail in section 4.2.

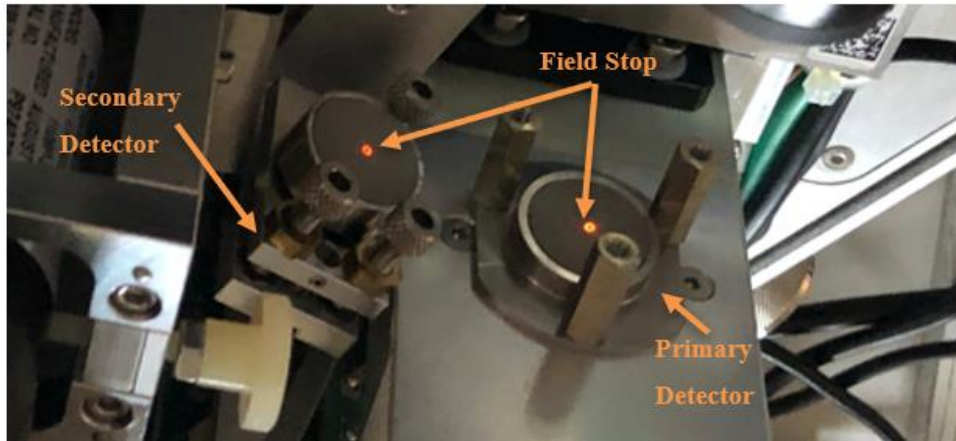


Figure 3.4. The completed diameter of the spectrometer's field stops is fully illuminated by the source's image (i.e., orange light).

3.3 Atmospheric Retrieval Strategy

In this thesis, Bruker OPUS software was utilized to control the spectrometer, record the interferograms and Fourier-transform their interference signals into the corresponding atmospheric spectra. The gas information at a specific spectral range is then analysed in-depth using the LINEFIT program, which was developed by Hase et al. (1999) and has been widely used for ILS determination. With the open-path approach, LINEFIT Version 14.9 is useful for characterizing the ILS profile and retrieving the column amount of the observed gases.

Before running LINEFIT, a set of input parameters must be defined first in the input script. This includes atmospheric quantities such as temperature, pressure and the length of open-path measurements, as well as the auxiliary parameters (e.g., ILS parameters...) and reference spectral information of the target gases (e.g., positions, intensities, broadenings...) dedicatedly measured in the laboratory. This study utilized the spectroscopic line lists offered by the HITRAN database (version 2020). LINEFIT will first generate the transmission spectrum of the target gas based on those inputs and then fit the measured spectrum to its spectral version, thereby retrieving the gas's spectral profile. The proper setup of the data analysis (i.e., spectral windows, type of gases, values of pressure, temperature, specification of ILS and fit strategy) is crucial for achieving the best estimate of the target gas column amounts.

3.4 Computation of Column-averaged Dry-air-mole Fractions

As the column amount of the atmospheric molecules is influenced by the variability of the ground pressure at the surface, the actual concentration should be specified as a column-averaged dry-air mole fraction to compensate for the dependency of the gas abundances on the effect of ground

pressure. Here, the retrieved total column of target abundance is converted into dry-air mole fraction by:

$$\text{X-Gas (ppm)} = \frac{\text{Gas}^{\text{Col}}}{\text{Dry-Air}^{\text{Col}}} \cdot 10^6 \quad (3.4)$$

X-Gas represents the column-averaged dry-air mole fraction of the target gas and $\text{Gas}^{\text{Col}} \left(\frac{\text{molec}}{\text{m}^2} \right)$ is its total column. $\text{Dry-Air}^{\text{Col}} \left(\frac{\text{molec}}{\text{m}^2} \right)$ is the total column of dry air, which is defined as:

$$\text{Dry-Air}^{\text{Col}} = \left[\frac{7.243 \cdot 10^{22} \cdot p(z) \cdot l}{T} - \text{H}_2\text{O}^{\text{Col}} \right] \quad (3.5)$$

Here, $p(z)$ (Pa) is the pressure at the altitude where the measurement takes place as compared to the reference altitude (see Eq. (2.3)), T ($^{\circ}\text{K}$) is the temperature surrounding the measurement area, and l (m) is the distance between the light source and the spectrometer. $\text{H}_2\text{O}^{\text{Col}} \left(\frac{\text{molec}}{\text{m}^2} \right)$ is the total column of water vapour, which is also retrieved from the open-path spectrum. In Eq. (3.6) which defines the number density $n \left(\frac{\text{molec}}{\text{m}^3} \right)$, $N_A = 6.022 \cdot 10^{23} \left(\frac{\text{molec}}{\text{mol}} \right)$ is Avogadro's number and $R = 8.314 \left(\frac{\text{J}}{\text{mol} \cdot \text{K}} \right)$ is the universal gas constant, giving the number $7.243 \cdot 10^{22} \left(\frac{\text{molec} \cdot \text{K}}{\text{J}} \right)$ in Eq. (3.5) (Berman, 2014).

$$n = \frac{N_A}{R} \cdot \frac{p}{T} \quad (3.6)$$

4 Ground-based CO₂ Measurement Sessions

Section 4.1 describes the first open-path CO₂ measurements conducted for a full weekend from 17:00 on the 27th, May 2022 to 15:00 on the 29th, May 2022 (~ 46 hours), while section 4.2 illustrates the second performance on the 12th, August 2022 at a much longer pathlength from 14:00 to 16:00 and 17:00 to 18:00 (3 hours). Two setups were carried out on this day, with and without the integration of an additional telescope system. In this chapter, the spectroscopic calculated temperatures and the derived dry-air-mole CO₂ concentrations measured by the open-path approach were compared and interpreted with the in-situ ICOS reference data.

4.1 Indoor Session: full weekend measurement from the 27th of May 2022 to the 29th of May 2022

4.1.1 MEASUREMENT SETUP

The optical setup of open-path CO₂ measurement is illustrated schematically in Fig. 4.1. The light source unit and EM27/SUN spectrometer (SN84) were located indoor on the 7th floor of the IMK-ASF Institute (KIT Campus North, building 435 with the coordinates of 49.094 °N and 8.4336 °E) at 134 m a.s.l (30 m above ground). The distance between the spectrometer and the light source was approximated to the length of the hallway of 21.8 m. Considering the vertical path of the first tracking mirror to the spectrometer's entrance (i.e., 33 cm), the total length is 22.13 m. The balcony door on the 7th floor was opened during the whole process so that the air inside the building is well-mixed with the outside. To control the light source intensity, a stabilized DC power supply was used. Even illumination of the light source onto the first mirror tracker can be achieved by adjusting the position of the source unit and the position of the trackers. Under this pathlength, the required image size is 10.4 cm and is lower than the applied source's size of 27.4 cm, thereby the source's image can be formed homogeneously onto the field stop.

The measured CO₂ spectra were hourly binned to compare with the reference data given by the ICOS tower (coordinate 49.0915 °N and 8.4249 °E) at 110 m a.s.l (200 m above the ground)¹. At Karlsruhe tall tower site, ICOS uses a cavity ring-down spectrometer (CRDS, Picarro, model G2301) which applies an in-situ approach to measure the temperature and dry-air-mole fraction of CO₂ and CH₄ at four altitudes: 30 m, 60 m, 100 m and 200 m above the ground. Based on the

¹ <https://www.icos-infrastruktur.de/icos-d/komponenten/atmosphaere/observatorien/karlsruhe-c1/>

altitude difference between the two measurement sites, the reference temperature and CO₂ datasets measured at 30 m were selected as the reference. The ICOS reference pressure measurements are recorded at 2.5 m above the ground. Hourly pressure values were used to calculate the path-averaged pressure (see section 4.1.2).

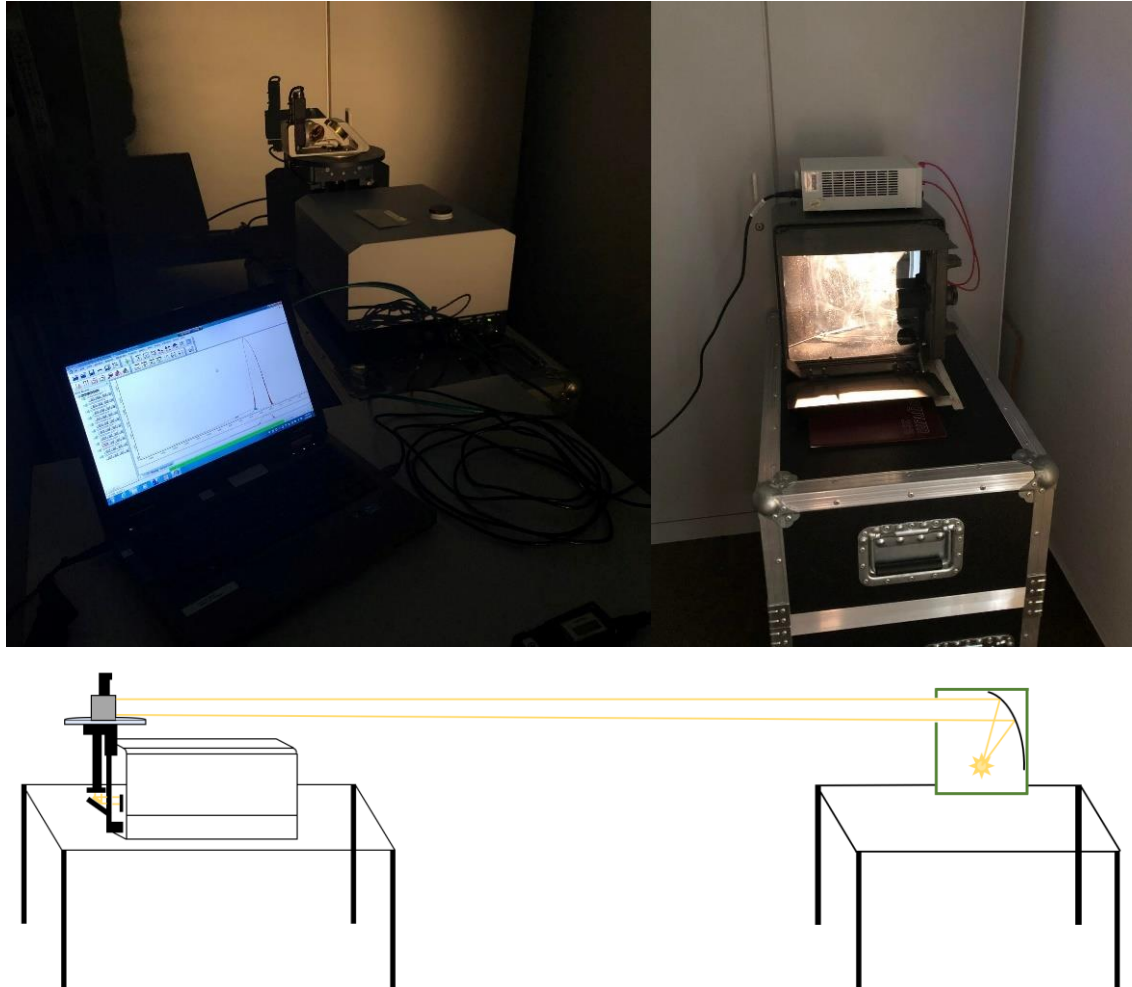


Figure 4.1. The top right and left panels are pictures of the spectrometer and light source taken during the measurement. The bottom panel is the schematic drawing of the setup where CO₂ concentrations were measured in between the optical pathlength.

4.1.2 INSTRUMENTAL LINE SHAPE (ILS) SELECTION FOR DATA ANALYSIS

For the open-path analysis, it is sufficient to use a simple ILS model with two empirical parameters (ME and PE) as the ILS shape of the EM27/SUN spectrometer is expected to be close to the nominal shape of an ideal Fourier Transform interferometer. Two selection methods of ILS were applied for the same CO₂ datasets: nominal ILS (mode 4) and open-path ILS (mode 3). From the latest ILS characterization for EM27/SUN spectrometer (SN84), mode 4 uses the C₂H₂-calibrated ME value of 1.010 and PE value of 0.0008411 rad for deriving the XCO₂ concentrations of all time series. On the other hand, as the ILS is expected to be stable on longer time scales, mode 3 includes the spectrum-derived ME and PE parameters as fit variables for hourly measurements. However, this

approach would also rely heavily on the noise level of the measured CO₂ spectrum. Depending on the presence of noise level and the signal intensity of the target absorption band in the open-path spectra, the spectrum-to-spectrum variability of generated ME and PE values of mode 3 can indicate a considerable uncertainty of the retrieved ILS (see Fig. 4.6).

4.1.3 INTRADAY VARIABLE OF PATH-AVERAGED TEMPERATURE AND PRESSURE MEASUREMENTS

As mentioned briefly in section 3.3, for the spectral analysis and the derivation of dry-air-mole fractions, LINEFIT requires precise information on the atmospheric physical quantities (i.e., open-path pressure and temperature) to create modelled spectra. As both atmospheric temperature and pressure are constantly changing throughout the measurement duration, one needs to account for the intraday variability of the temperature-pressure profile while evaluating the retrieved data. There are two ways to determine the temperature values for open-path measurements: either use the temperature measured by dedicated in-situ devices at a certain position along the path, or include retrieval of temperature as a fit variable in the analysis of the observed spectra. However, performing the first method is inefficient in obtaining the mean effective pressure-temperature profile, as external background factors (e.g., solar radiation and thermal mass in the surrounding open-path environment) can impact and vary the temperature at any points along the path (Deutscher et al. 2021). For minimizing a possible bias due to incorrect temperature determination, the second method of fitting the temperature was chosen for the thesis analysis.

Using Eq. (2.3), the pressure surrounding the measurement area was calculated based on the ICOS reference ground pressure and the reference temperature at 30 m above the ground. This results in lower open-path pressure values, as the spectrometer was located at a higher altitude than the ICOS pressure sensor (see Fig. 4.2). To derive the path-averaged temperature for every measurement hour, LINEFIT algorithm uses the ICOS reference temperature values at 30 m above the ground as the initial approximations to adjust the effective path-averaged temperature values in the least-squared fit from the CO₂ window at 4978 cm⁻¹. The retrieved spectrum-derived temperature data are then fixed and applied for the re-analyses of XCO₂ concentrations. Fig. 4.2 illustrates the path-averaged temperatures as deduced from mode 4 and mode 3 analysis. The same trend as the ICOS reference data is found, where the temperatures are higher during daytime and lower at night-time. Their difference ranges from 0 °C up to roughly 5 °C. There is a systematic offset, in that the path-averaged temperatures are higher than the ICOS in-situ point measurements. Since the open-path setup was realized along a corridor inside a building, despite the ventilation with open doors, being higher than ambient temperatures along the measurement path are plausible.

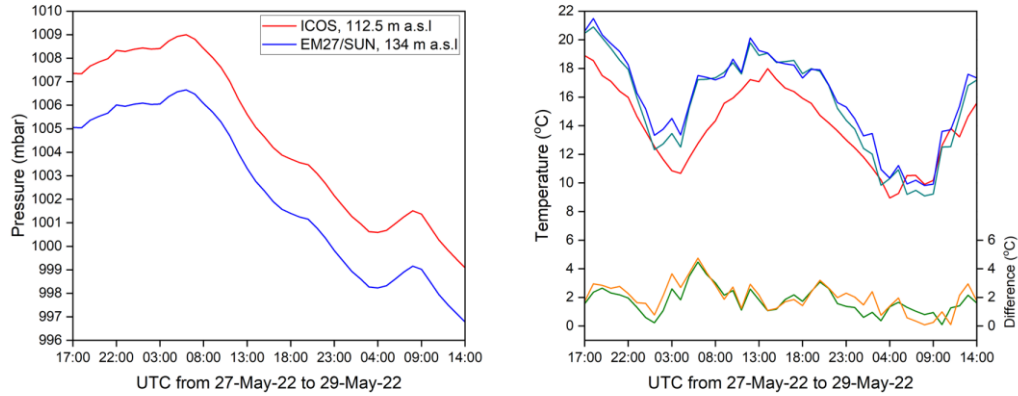


Figure 4.2. Left panel: the calculated open-path pressures and ICOS ground pressures. Right panel: temperature measured directly by ICOS tower (140 m a.s.l red) and spectroscopically derived temperature [LINEFIT fitting algorithm of mode 4 (134 m a.s.l, dark cyan) and mode 3 (134 m a.s.l, blue)]. The experimental and reference difference is illustrated by olive green (mode 4) and orange (mode 3) lines].

4.1.4 CO₂ CONCENTRATION RETRIEVALS

4.1.4.1 CO₂ Column

EM27/SUN spectrometer only measures the absorption bands of the target gas in the near-infrared region. Although the intensity of CO₂ bands in the mid-infrared spectrum is stronger than in the near-infrared region, which is advantageous for open-path measurement, different materials and detectors with an extra cooling system are required, making the instrumentation cumbersome and immobile. In this thesis, the spectral window in the range of 4910 cm⁻¹ to 5040 cm⁻¹ was applied for the near-infrared open-path analysis. To retrieve and evaluate the CO₂ column, LINEFIT fits the spectral region based on the atmospheric input quantities and HITRAN line parameters. Compared to the theoretical band of CO₂ shown in Fig. 2.7, the result of additional peaks is due to the interference with water lines in the same spectral range. The residual plot in Fig. 4.2 provides further information on the spectral structure, specifically the variations of the continuum backgrounds which is a potential error source in retrieving the total CO₂ column and its dry-air-mole fraction. The repeatable noise shown in the residual plot has a random pattern and provides some information on the signal-to-noise ratio (SNR) of the measured spectrum. High-intensity and structural residual means that there are background errors that can potentially affect the retrieval results and cause lower SNR quality to the recorded spectrum. The variations can come from the atmospheric origin, or the characteristics of the spectrometer's optical components (e.g., frequency dependence on the coating material of mirrors...) (Kiel, 2016). Fig. 4.3 presents the spectrum-averaged CO₂ band for all 46 hours with P-branch and R-branch. As expected, the mode 3 ILS analysis scheme (i.e., the ILS fit included) slightly reduces the fit residuals.

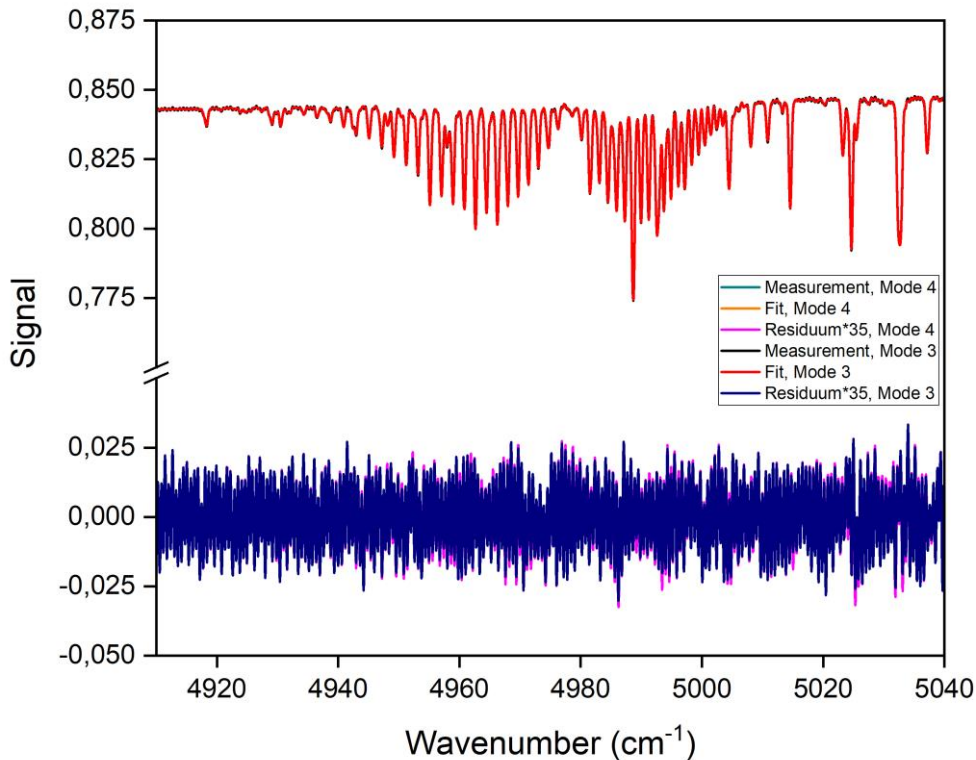


Figure 4.3. Illustration of three-days averaged band intensity of CO₂ in the spectral window with centred wavenumber at 4978 cm⁻¹ and the fit. Residual plots from modes 4 and 3 were multiplied by a factor of 100 to show their detailed structure.

4.1.4.2 XCO₂ Concentrations

Fig 4.4 shows the hourly XCO₂ concentrations retrieved using mode 3 and mode 4 strategies. The retrieved results of mode 3 are highly biased in comparison to the ICOS reference and appear to be noisier. One can observe that the data of mode 4 are in better agreement with the reference readings.

Both ICOS and the open-path measurements indicate the same diurnal variation. The dry-air-mole CO₂ concentrations are consistently higher at night-time and lower during the daytime, which can be due to the biosphere influence. Plant photosynthesis is only active in the presence of sunlight, thus respiration dominates during the night-time, resulting in a positive net flux of CO₂. While a strong atmospheric convective mixing across the PBL reduces vertical gradients in the CO₂ concentration profile, the nightly respiration signal is confined to the very shallow nocturnal boundary layer. From the geographic point of view, two measurement sites are evenly surrounded by trees and plants in the urban area; therefore, the variability of the XCO₂ concentration indicated by the two retrieval approaches was expected to be similar. However, a slight increase for mode 4 on the overall average and a prevalent rise for mode 3 are found for all time points. This is probably due to the residual bias of the open-path calibration in comparison to the ICOS reference (see

section 5.1). Another reason for the discrepancies between the ICOS reference and the open-path results might be the advection of CO₂ emissions from local sources (i.e., nearby coal and gas power plants, agriculture areas...), as they are not strictly co-located. Fig. 4.5 plots the wind speed and its direction according to the XCO₂ difference at all time points. It indicates that the wind coming from the north (e.g., Mannheim power station unit 9), from the northwest (e.g., nearest is the Bexbach-C power station Unit 1), from the southwest (e.g., Karlsruhe power station unit 7) and from the east (e.g., Heilbronn power station Unit 7) may give the potential rise to open-path data. The XCO₂ differences of both modes are highest for winds coming from the north direction.

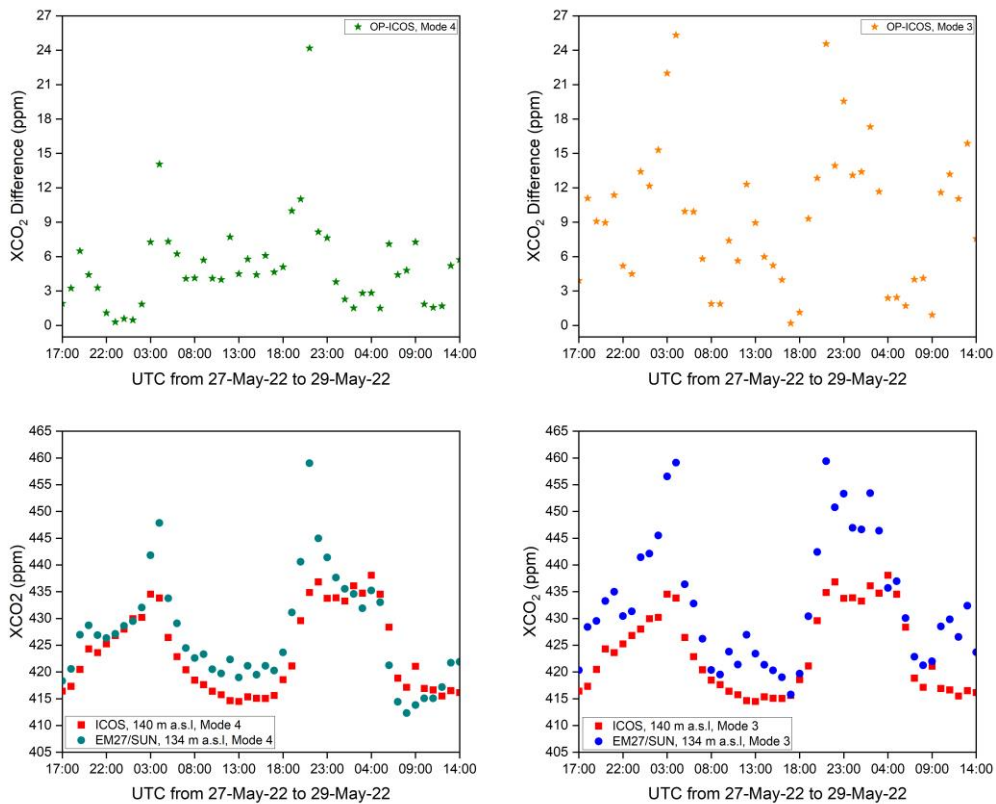


Figure 4.4. The comparison of XCO₂ concentration between open-path EM27/SUN and ICOS spectrometer, along with their differences stated in the top panel.

The pattern displayed in Fig. 4.4 suggests that the systematic background errors might be another factor to deviate the open-path XCO₂, such as the uncertainty in pathlength measurement, path-averaged temperature, pressure, HITRAN line parameters, as well as statistical noise. As those relative errors are presented by residual plot, the hours that recorded higher XCO₂ differences have higher residual intensity with repeatable patterns than those that recorded lower CO₂ differences.

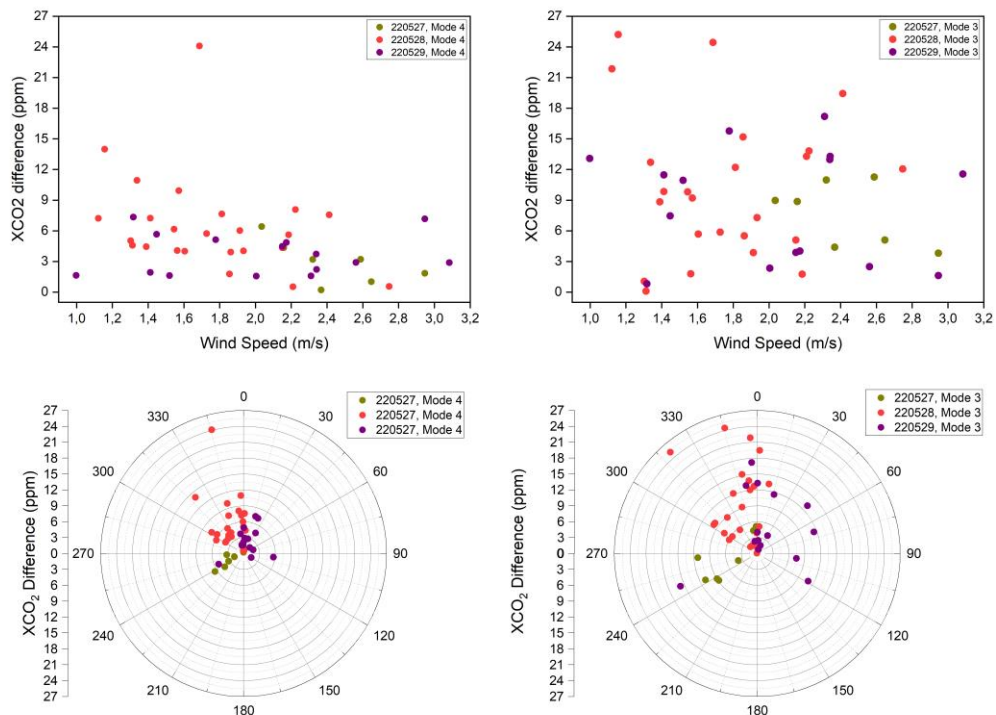


Figure 4.5. Wind speed and wind direction are plotted against the XCO₂ difference between the two modes.

Fig. 4.4 also demonstrates that the dry-air-mole CO₂ concentrations provided by mode 3 are significantly larger than the reference data, giving higher error than mode 4. This discrepancy is triggered by the fact that the ILS retrieval from the noisy CO₂ band suggests lower ME values than the cell measurement suggests. If the modelled spectral lines are broader, the fit to a measured spectrum will indicate higher columns.

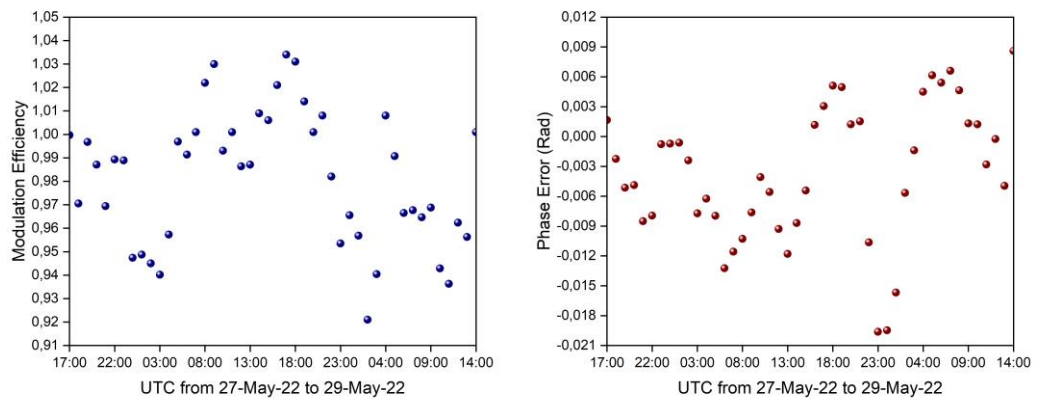


Figure 4.6. Fluctuated ME and PE values generated by the LINEFIT algorithm of mode 3 for all time points.

4.2 Outdoor Session: weekday measurement on the 12th of August 2022

4.2.1 MEASUREMENT SETUP

The open-path measurements were performed outdoor on the ground level at 112 m a.s.l and were located in the area next to building 435 on the Weingartener Straße (see Fig. 4.8). Both EM27/SUN spectrometer (SN84) and the light source unit were carried to the measurement site using a trolley. The path length of 114.65 m between the two main components was measured by a laser distance meter, giving a total distance of 114.98 m from the vertical distance of the first tracking mirror to the spectrometer's entrance of 33 cm. Since the measurements were performed during a sunny day, the presence of non-negligible reflective and scattering background light coming from the Sun was tested by recording the signals without turning on the light source unit. The detected signals would then be subtracted from the original CO₂ signals with the light source on. Fortunately, no background signal was detected. For the first two hours, the optical setup was kept the same as previously mentioned in subsection 4.1.1, while an additional telescope system (Vixen, 80/900 achromatic refractor) was integrated for the third hour. The telescope has an aperture diameter of 80 mm, the objective's and eyepiece's focal length of 900 mm and 100 mm which gives the overall magnification of 9x using Eq. (3.4). Here, the telescope was positioned toward the tracking mirror such that the source's image was seen to illuminate the field stop. With the increase of overall magnification of the optical system, Eq. (3.1) and (3.2) recalculate the maximum image size and the corresponding distance in section 3.2, which were determined to be smaller or equal to $9x \cdot G = 246.6 \text{ cm}$ and 523.3 m , respectively. In this case, the demanded image size for a homogeneous illumination onto the spectrometer's FOV is roughly 6 cm and is much smaller than the source's size, thereby fulfilling the condition shown in Fig. 4.7.



Figure 4.7. With the insertion of the telescope system, the spectrometer's FOV is illuminated fully by the source at distance farther than the initially speculated pathlength in section 3.2.



Figure 4.8. The optical setup with a telescope system in between the spectrometer (left) and the light source (right) for CO₂ open-path measurement.

4.2.2 MEASUREMENT RESULTS

For the analysis, the ICOS reference temperature and pressure values measured at 2.5 m above the ground (112.5 m a.s.l) were considered for calculating and deriving the path-averaged pressure and temperature of the open-path approach. The closest reference XCO₂ concentrations quantified at 30 m above the ground (140 m a.s.l) were taken for further comparison. The retrieval process used the same strategy as for the previous measurements, but only mode 4 was applied as the main ILS selection method due to the lower quality of mode 3 detected previously. Table 1 below summarises the open-path pressures calculated using Eq. (2.3) and additional wind information at 30 m above the ground for three-hour measurements.

Table 1. Summary of the calculated open-path pressures based on ICOS reference pressures and relevant wind information.

Time, UTC on 12 th , August 2022	ICOS Pressures (mbar) at 112.5 m a.s.l	ICOS Wind Speed ($\frac{m}{s}$) at 140 m a.s.l	ICOS Wind direction ($^{\circ}$) at 140 m a.s.l	Open-path EM27/SUN Pressures (mbar) at 112 m a.s.l
14:00	1002.48	2.708	58.471	1002.628348
15:00	1002.26	2.433	66.608	1002.409184
17:00	1002	2.063	73.346	1002.155513

Fig. 4.9 demonstrates the path-averaged temperatures (left panel) and the calculation of XCO₂ concentrations (right panel) with LINEFIT software. A good agreement with the ICOS reference is found for the retrieved temperature. A moderate-high bias at 15:00 might be because the open-path measurements crossed an asphalt road that is prone to heating by solar insolation. The level of agreement found for XCO₂ is also quite good, on the 1 ppm level. The additional use of the telescope system yields a significant improvement in the spectral SNR, which is also illustrated by the residual plot for each measurement hour in Fig. 4.9.

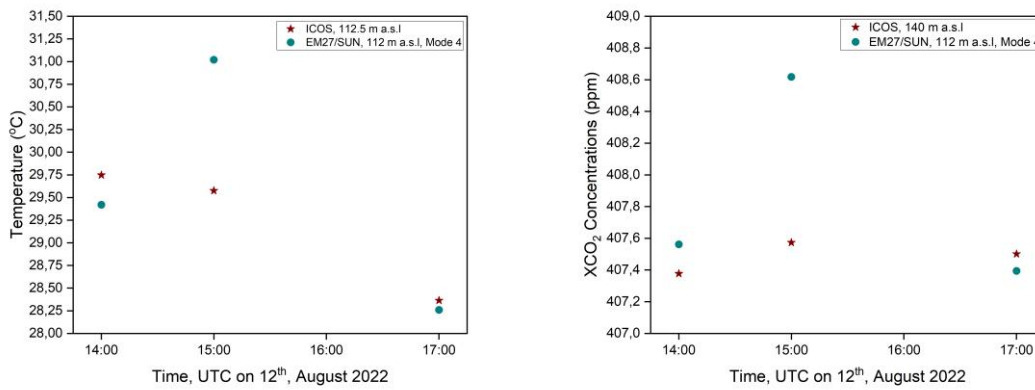


Figure 4.9. Spectroscopic spectrum-derived temperatures (left panel) and the calculation of dry-air-mole XCO₂ fractions (right panel).

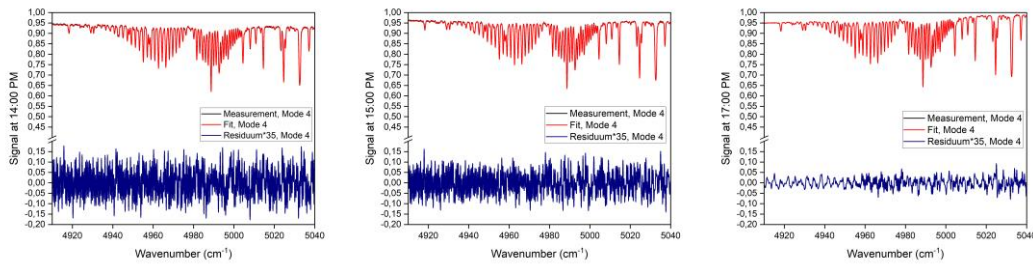


Figure 4.10. Spectra and residual signals of each measurement hour.

5 Discussion

The goal of this chapter is to test and assess the measurement quality of the full weekend open-path setup from section 4.1, as well as to evaluate the error budgets such that a more optimum plan can be carried out for future measurements.

5.1 Error Budgets for Open-path CO₂ Measurements

The retrieval of trace gas concentrations is always subjected to various error sources. In addition to the external factors (i.e., wind and altitude difference) that could potentially disturb the open-path results in the aforementioned chapter, systematic and statistical uncertainties should be accounted for. Those spectroscopic uncertainties are determined to evaluate the influence on the retrieval column amounts and the corresponding deviations from the reference data. Two major types are studied in this thesis: statistical uncertainties (e.g., spectral noise...), and the systematic uncertainties that cause persistent biases with respect to the true measurement value (e.g., spectroscopic data, assumed path length, incorrect calibration of pressure sensor...). Systematic errors display strong correlations between the individual lines, while statistical errors are most likely uncorrelated. For different uncertainty sources, the correlative influences on the final CO₂ concentration are different (Birk et al. 2021).

The EM27/SUN measured higher concentrations than the ICOS reference readings, giving an averaged statistical difference of $(0.8 \pm 0.03) \%$ and $(2.1 \pm 0.1) \%$ for modes 4 and 3 respectively. There is a significant offset between the open-path and the in-situ approaches, resulting in the calibration factor of 1.05917 ± 0.10657 for mode 4 and 1.36522 ± 0.11036 for mode 3 (see Fig. 5.1). The slopes of the two modes are within the 1σ precision range of the dataset. As mentioned, many uncertainties could potentially affect the final open-path results. The HITRAN2020 line parameters (i.e., line strength and line pressure broadening) are one of the important contributions to the systematic error budget and are accounted for in this section. Other dominant error sources are the measured pathlength, pressure, path-averaged temperature, ILS, as well as statistical spectral noise will also be targeted for the investigation.

For the CO₂ band of 20012←00001, the relative uncertainties of the HITRAN2020's pressure broadening half width and its corresponding temperature dependency were reported to be in the range from 2 % to 5 %, while the error range of $\geq 1 \%$ and $< 2 \%$ was derived for line intensity (Gordon et al. 2022). In addition to the effect of pressure, the transition lines can also be broadened by another uncertainty factor caused by the collision with H₂O. The contribution of H₂O as a

collision partner to the broadening of CO₂ lines should be considered, especially when the measurements take place in the troposphere where the water amount is significant. Water vapour can broaden the CO₂ lines more effectively than other collision partners, as it has a higher cross-section due to strong polarity and is lighter. To account for this effect as a percentage error, the pressure values for all time points were re-calculated using Eq. (5.1). However, this effect was calculated to be small in comparison to other sources of uncertainty, thereby can be neglected in the final analysis.

$$P_{\text{effect}} \approx P_{\text{measure}} \cdot \left(1 + 0.3 \cdot \frac{H_2O^{\text{Col}}}{\text{Dry-Air}^{\text{Col}}} \right) \quad (5.1)$$

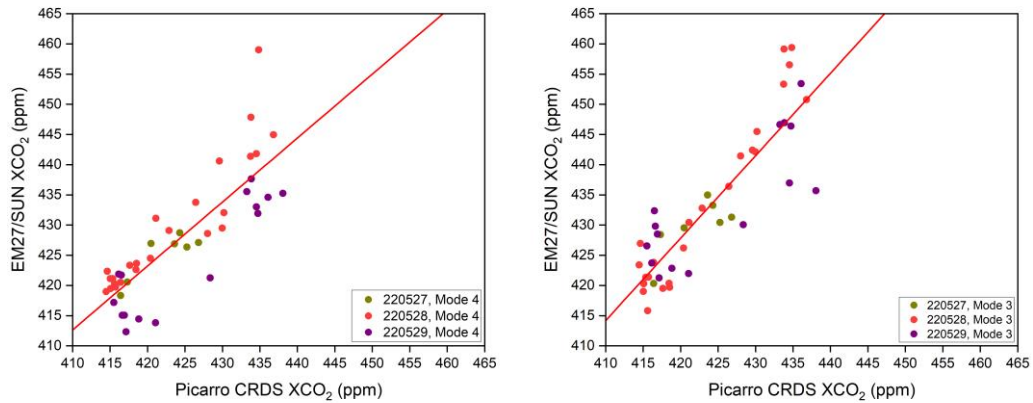


Figure 5.1. XCO₂ comparison between the EM27/SUN spectrometer with the ICOS CRDS.

The deviation that the laser distance meter can make while measuring the pathlength from the lamp window to the spectrometer’s first tracking mirror is estimated to be ± 0.1 m. However, since the internal distance between the optical components (i.e., from the off-axis mirror to the lamp window) within the light source unit was unknown and not included in the XCO₂ calculations, this approximates the total deviation of (22.13 ± 0.15) m. For the calculated pressure, it is estimated to be on the order of 0.2 % as compared to the ICOS ground pressure. The average difference between the spectroscopic spectrum-derived temperatures and ICOS reference readings for all the time points is (1.5 ± 0.75) °C for mode 4 and (1.95 ± 0.5) °C for mode 3.

The column-average dry-air-mole fractions of CO₂ and path-averaged temperature can be under- or over-estimated based on the assumption of ILS line shape. An ideal ILS with unity ME which deviates 1 % from the used C₂H₂-calibrated ME amplitude (i.e., ME = 1.01) delivers an over-estimated XCO₂ concentration on the order of 0.5 % and temperature of 0.15 °C for mode 4. Therefore, with the use of mode 4, the measured XCO₂ spectra for all hours should not be affected by the error source that originates from the co-retrieved ILS parameters. Since the ME values of

the mode 3 analysis were strongly influenced by the presence of random noise, hourly changes of retrieved ME would disturb the XCO₂ differently. On average, a 1 % change in ME leads to roughly a 1 % error in the measured CO₂ concentration for each hour.

To account for the statistical noise error, the SNR from the ratio of two consecutive spectra in the hour of 23:00 on the 27th May 2022 and at 21:00 on the 28th May 2022 were analysed with modes 4 and 3. This is because 23:00 and 21:00 yield the least and most deviated XCO₂ concentration as compared with the ICOS readings among all other open-path results, thereby estimating the uncertainty range of spectra SNR and its impact on the measured CO₂ mole fractions. Ten consecutive spectra were selected, and the root-mean-square (RMS) of the fit residual given by the division of a consecutive pair was calculated in the range from 4910 cm⁻¹ to 5040 cm⁻¹. A parabolic fitting was applied beforehand. The delivered RMS value was then multiplied by $\sqrt{2}$ to determine the SNR of a single spectrum. Ten corresponding XCO₂ values from those spectra were analysed to compute the standard deviation, which was then divided by $\sqrt{10}$ to conclude the XCO₂ error bar for each spectrum due to the spectral noise. Hypothetically, it is estimated that the SNRs of all CO₂ spectra and their influence on XCO₂ mole fractions only vary within the given range.

Seven important uncertainties were summarized in Table 2, along with their impact on the final XCO₂ measurements:

Table 2. Leading error sources that influence the retrieved CO₂ mole fractions for the full weekend session. To assess the impact of the pathlength, temperature, pressure, HITRAN's line intensity and pressure broadening uncertainties on the analytical results, XCO₂ values of all hours were recalculated based on the change, analysed under mode 4 and 3 strategies, and compared with the original open-path XCO₂ concentrations.

	Uncertainty	Resulting error (%) on the measured XCO ₂ (mode 4)	Resulting error (%) on the measured XCO ₂ (mode 3)
Pathlength	± 0.15 m	(0.7 ± 0.042) %	(0.7 ± 0.05) %
Temperature	± 1.5 °C (mode 4) ± 1.95 °C (mode 3)	(0.52 ± 0.02)%	(0.68 ± 0.04) %
Pressure	± 0.2 mbar	(0.02 ± 0.00093)%	(0.02 ± 0.0011) %
HITRAN Pressure broadening	± 2 % (equivalent to a pressure error of ± 20 mbar)	(1.29 ± 0.06)%	(2.1 ± 0.11) %
HITRAN Line intensity	± 1 %	(1 ± 0.05) %	(1 ± 0.06) %
ME/ILS	1 %	-	1 %
Statistical spectra SNR	(2403 ± 119.75) to (2517 ± 104.75)	0.8 % to 1.17 %	0.93 % to 1.33 %

5.2 Possible Further Improvements on the Optical Setup

5.2.1 TELESCOPE

In comparison to a reflecting telescope, a refracting model has some disadvantages. The major downside results from the dispersive characteristic of the lens due to its dependency on the material's refractive index. This generates chromatic aberration that distorts the symmetry of the ILS shape. Therefore, the application of a larger reflecting telescope for future open-path measurements would be desirable. A reflector also enables twice the pathlength offered by the refracting system. One approach is to acquire a reflecting telescope (i.e., the Cassegrain model contains two main components: a parabolic primary mirror and one hyperbolic secondary mirror) to be placed on top of the spectrometer (see Fig. 5.2, inspired from Merten et al. (2011)). The size of the final formed image of the light source should be larger or at least equal to the size of the field stop of the EM27/SUN spectrometer. Taking the reference distance of 1.5 km as an example (total round trip is ~ 3 km), which is required for the measurement of atmospheric CO₂, CH₄, H₂O and O₂ bands in the near-infrared region (Griffith et al., 2018), Eq. (3.1) and (3.2) are combined to estimate a range that the telescope's magnification should have:

$$707.46 \text{ (cm)} \leq M \cdot G \quad (5.2)$$

If one keeps the same beam size of 27.4 cm as in the thesis's previous measurement, the required hypothetical image size for a 1.5 km path measurement can be reduced by enhancing the telescope's magnification to at least 30x. For future implementation, the proposed focal lengths of the primary and secondary mirrors are 1500 mm and 50 mm respectively. From the position of the first tracking mirror, the secondary mirror should be placed within a distance that allows the spectrometer's FOV to capture the full image of the applied light source. From the production point of view, it is reasonable to have a diameter of 30 mm for this mirror. Moreover, the diameter of the primary mirror must be large enough to collect all the incoming parallel beams, thereby should be increased proportionally to the dimension of the applied light source. In this study, a diameter of 300 mm for the primary mirror is plausible. Furthermore, increasing the beam size by expanding the reflector's diameter is another option to relax the requirement in Eq. (5.2), as well as to realize a much longer pathlength than the reference distance given above.

Better beam collimation, lower measurement noise and repeatability enhancement can be achieved by increasing the area of the primary mirror and reflector, as well as with the use of a higher brightness source (Griffith et al., 2018). While performing the open-path measurements with this setup, the alignment and orientation between the main optical components must be precise, highly accurate and well-defined, especially the secondary mirror which guides the light to the first tracking mirror. The additional misalignment which might be generated from the thermal or

mechanical disturbances should be accounted for in the final analysis, since ill-alignment between the optical components can lead to a considerable loss of signal.

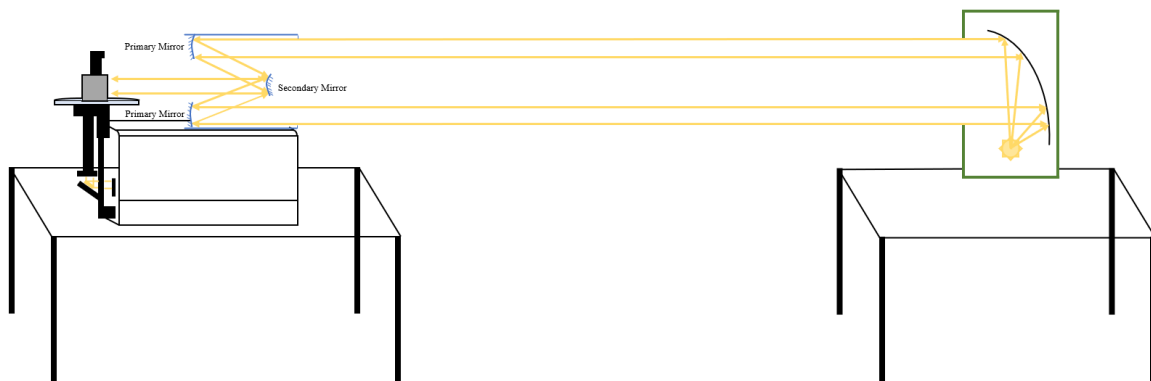


Figure 5.2. The proposed setup for open-path EM27/SUN for achieving longer pathlength.

5.2.2 LIGHT SOURCE

The light source used in this thesis was an incandescent tungsten-halogen light source. For the purpose of measuring the GHGs at night-time, using a near-infrared light-emitting diode (LED) with a broadband spectrum is more beneficial than an incandescent bulb. LED requires much less power to operate and has a higher lifetime, but still offers the same brightness and higher efficiency. Moreover, a near-infrared LED does not attract as many insects as the incandescent source during the night-time. The selected light source should be compatible with the detectors and tracker of the EM27/SUN spectrometer, where the LED must operate in continuous wave mode and offer the optical output power that is sufficient for detection. To the current knowledge, the commercial available LEDs were mostly manufactured for measuring CH_4 and stronger CO_2 bands in the mid-infrared region. However, many studies on the fabrication of LED light source that are suitable for the research's needs were conducted in the past. One of the greatest sources of information is the research made by Prineas et al. (2006), where they described their step-by-step process of fabricating LEDs (i.e., $2 \mu\text{m} \leq \lambda \leq 2.5 \mu\text{m}$) with the continuous wave output at room temperature. By stacking multiple active regions of GaInAsSb semiconductor, their cascaded LED show higher efficiency but still requires lower total current input than single-state LED devices. For better enhancements on the quality of the open-path measurements, this type of LED light source is hoped to be commercialized in the near future.

6 Conclusion

In conclusion, monitoring anthropogenic emissions is an important mission to understand the greenhouse effect and its consequence on future climate behaviour. Compared to other remote-sensing techniques, the use of the ground-based FTIR spectrometer has been a great contributor to determining the local source and sink of the target gas with high precision and accuracy. Based on the CO₂ bands of 3001x, Birk et al. (2021) reported the FTS method could deliver a combined uncertainty of 0.15 %, and it is feasible to achieve lower uncertainty of 0.1 % with additional implementations.

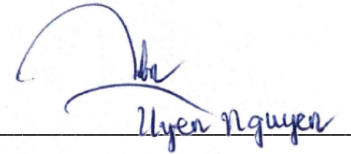
EM27/SUN FTIR spectrometer is a robust, reliable, and highly accurate instrumentation for the measurements of GHGs using the Sun as the main light source. To enable EM27/SUN observations during night-time and under overcast conditions, this thesis focuses on configuring the open-path setup with an additional light source as the replacement of the Sun. As the first step of this research, a simple optical setup of only the source unit and the spectrometer was performed under a distance of 22.13 m measurement to assess the retrieval quality of dry-air-mole CO₂ fractions. For the analysis method, two different approaches of ILS selection were chosen (i.e., mode 4 and mode 3). On a three-day average, the column-averaged CO₂ dry-air-mole fractions retrieved from the open-path measurements showed differences of (0.8 ± 0.03) % for mode 4 and (2.1 ± 0.1) % for mode 3 as compared to the ICOS reference readings. Mode 3 gave the more fluctuated and unreliable results than mode 4, as it is affected by the low SNR quality of the recorded spectra. One can obtain a higher signal level and reduce the uncertainty in pathlength by implementing the measurement at a longer distance and with a higher source's brightness.

The use of the Vixen refractor has helped one to achieve a much better SNR quality at a longer path observation and is greatly beneficial for measuring weak CO₂ bands. As the next step of this research, open-path measurements with the refracting telescope could be performed again for a longer time period to obtain the overall quantitative observations on the retrievals and to also account for error sources as compared with the previous setup. For future research, it is recommended to use a larger reflecting telescope, and to replace the incandescent light bulb with a near-infrared broadband LED source. This would deliver higher long-term efficiency and higher SNR spectra than the refracting system.

7 Declaration of Academic Integrity

I herewith declare that the present thesis is original work written by me alone, that I have indicated completely and precisely all aids used as well as all citations, whether changed or unchanged, of other theses and publications, and that I have observed the KIT Statutes for Upholding Good Scientific Practice, as amended

Karlsruhe, the 31st of October 2022

A handwritten signature in blue ink, appearing to read 'Uyen Nguyen', is written over a horizontal line. The signature is stylized with a large loop at the beginning.

First name Last name

Bibliography

Alberti, C., Hase, F., Frey, M., Dubravica, D., Blumenstock, T., & Dehn, A. et al. (2022). Improved calibration procedures for the EM27/SUN spectrometers of the COllaborative Carbon Column Observing Network (COCCON). *Atmospheric Measurement Techniques*, 15(8), 2433-2463. <https://doi.org/10.5194/amt-15-2433-2022>

Atkins, P., & Paula, J. (2014). *Atkins' Physical Chemistry* (8th ed., pp. 430-464). Oxford University Press.

Berman, A. (2014). *Vacuum Engineering Calculations, Formulas, and Solved Exercises* (p. 3). Academic Press, Inc.

Birk, M., Röske, C., & Wagner, G. (2021). High accuracy CO₂ Fourier transform measurements in the range 6000–7000 cm⁻¹. *Journal Of Quantitative Spectroscopy And Radiative Transfer*, 272, 107791. <https://doi.org/10.1016/j.jqsrt.2021.107791>

Boesch, H., Liu, Y., Tamminen, J., Yang, D., Palmer, P., & Lindqvist, H. et al. (2021). Monitoring Greenhouse Gases from Space. *Remote Sensing*, 13(14), 2700. <https://doi.org/10.3390/rs13142700>

Chen, J., Viatte, C., Hedelius, J., Jones, T., Franklin, J., & Parker, H. et al. (2016). Differential column measurements using compact solar-tracking spectrometers. *Atmospheric Chemistry And Physics*, 16(13), 8479-8498. <https://doi.org/10.5194/acp-16-8479-2016>

Davis, S., Abrams, M., & Brault, J. (2001). *Fourier Transform Spectrometry* (p. 67). Academic Press.

Deutscher, N., Naylor, T., Caldow, C., McDougall, H., Carter, A., & Griffith, D. (2021). Performance of an open-path near-infrared measurement system for measurements of CO₂ and CH₄ during extended field trials. *Atmospheric Measurement Techniques*, 14(4), 3119-3130. <https://doi.org/10.5194/amt-14-3119-2021>

Eismann, M. (2012). *Hyperspectral Remote Sensing* [Ebook] (pp. 363-394). SPIE Press. Retrieved 5 July 2022, from <https://doi.org/10.1117/3.899758>.

Frey, M., Hase, F., Blumenstock, T., Groß, J., Kiel, M., & Mengistu Tsidu, G. et al. (2015). Calibration and instrumental line shape characterization of a set of portable FTIR spectrometers for detecting greenhouse gas emissions. *Atmospheric Measurement Techniques*, 8(7), 3047-3057. <https://doi.org/10.5194/amt-8-3047-2015>

- Frey, M., Sha, M., Hase, F., Kiel, M., Blumenstock, T., & Harig, R. et al. (2019). Building the Collaborative Carbon Column Observing Network (COCCON): long-term stability and ensemble performance of the EM27/SUN Fourier transform spectrometer. *Atmospheric Measurement Techniques*, 12(3), 1513-1530. <https://doi.org/10.5194/amt-12-1513-2019>
- Friedlingstein, P., Jones, M., O'Sullivan, M., Andrew, R., Bakker, D., & Hauck, J. et al. (2022). Global Carbon Budget 2021. *Earth System Science Data*, 14(4), 1917-2005. <https://doi.org/10.5194/essd-14-1917-2022>
- Gisi, M., Hase, F., Dohe, S., & Blumenstock, T. (2011). Camtracker: a new camera controlled high precision solar tracker system for FTIR-spectrometers. *Atmospheric Measurement Techniques*, 4(1), 47-54. <https://doi.org/10.5194/amt-4-47-2011>
- Gisi, M., Hase, F., Dohe, S., Blumenstock, T., Simon, A., & Keens, A. (2012). XCO₂-measurements with a tabletop FTS using solar absorption spectroscopy. *Atmospheric Measurement Techniques*, 5(11), 2969-2980. <https://doi.org/10.5194/amt-5-2969-2012>
- Gordon, I., Rothman, L., Hargreaves, R., Hashemi, R., Karlovets, E., & Skinner, F. et al. (2022). The HITRAN2020 molecular spectroscopic database. *Journal Of Quantitative Spectroscopy And Radiative Transfer*, 277, 107949. <https://doi.org/10.1016/j.jqsrt.2021.107949>
- Griffioen, N. (2021). *Development of CO₂-O₂ CARS thermometry and concentration measurements for applied flame diagnostics* (M.Sc.). Delft University of Technology.
- Griffith, D., Pöhler, D., Schmitt, S., Hammer, S., Vardag, S., & Platt, U. (2018). Long open-path measurements of greenhouse gases in air using near-infrared Fourier transform spectroscopy. *Atmospheric Measurement Techniques*, 11(3), 1549-1563. <https://doi.org/10.5194/amt-11-1549-2018>
- Gulev, S., Thorne, P., Ahn, J., Dentener, F., Domingues, C., & Gerland, S. et al. (2021). *Climate Change 2021: The Physical Science Basis report*. (pp. 300-301). IPCC Sixth Assessment Report - Working Group I: The Physical Science Basis. Retrieved from <https://www.ipcc.ch/report/ar6/wg1/>
- Haradhan, M. (2011). Dangerous effects of methane gas in atmosphere. *International Journal Of Economic And Political Integration*, 1(2), 3-10. Retrieved 25 May 2022, from <https://mpira.ub.uni-muenchen.de/50844/>
- Harris, D. (2015). *Quantitative Chemical Analysis* (8th ed., p. 395). WH Freeman.
- Hase, F., Blumenstock, T., & Paton-Walsh, C. (1999). Analysis of the instrumental line shape of high-resolution Fourier transform IR spectrometers with gas cell measurements and new retrieval software. *Applied Optics*, 38(15), 3417. <https://doi.org/10.1364/ao.38.003417>

- Hase, F., Frey, M., Blumenstock, T., Groß, J., Kiel, M., & Kohlhepp, R. et al. (2015). Application of portable FTIR spectrometers for detecting greenhouse gas emissions of the major city Berlin. *Atmospheric Measurement Techniques*, 8(7), 3059-3068. <https://doi.org/10.5194/amt-8-3059-2015>
- Hase, F., Frey, M., Kiel, M., Blumenstock, T., Harig, R., Keens, A., & Orphal, J. (2016). Addition of a channel for XCO observations to a portable FTIR spectrometer for greenhouse gas measurements. *Atmospheric Measurement Techniques*, 9(5), 2303-2313. <https://doi.org/10.5194/amt-9-2303-2016>
- Hedelius, J., Viatte, C., Wunch, D., Roehl, C., Toon, G., & Chen, J. et al. (2016). Assessment of errors and biases in retrievals of XCO₂, XCH₄, XCO, and XN₂O from a 0.5 cm⁻¹ resolution solar-viewing spectrometer. *Atmospheric Measurement Techniques*, 9(8), 3527-3546. <https://doi.org/10.5194/amt-9-3527-2016>
- Hollas, J. (2004). *Modern Spectroscopy* (4th ed., pp. 103-151). John Wiley & Sons Ltd.
- Jain, P. (1993). Greenhouse effect and climate change: scientific basis and overview. *Renewable Energy*, 3(4-5), 403-420. [https://doi.org/10.1016/0960-1481\(93\)90108-s](https://doi.org/10.1016/0960-1481(93)90108-s)
- Jones, T., Franklin, J., Chen, J., Dietrich, F., Hajny, K., & Paetzold, J. et al. (2021). Assessing urban methane emissions using column-observing portable Fourier transform infrared (FTIR) spectrometers and a novel Bayesian inversion framework. *Atmospheric Chemistry And Physics*, 21(17), 13131-13147. <https://doi.org/10.5194/acp-21-13131-2021>
- Khan, Z. (2017). Causes and Consequences of Greenhouse Effect & Its Catastrophic Problems for Earth. *International Journal Of Sustainability Management And Information Technologies*, 3(4), 34. <https://doi.org/10.11648/j.ijsm.20170304.11>
- Kiel, M. (2016). *Trace gas measurements from different spectral regions using FTIR spectroscopy* (Ph.D). Institute of Meteorology and Climate Research - Atmospheric Trace Gases and Remote Sensing (IMK-ASF).
- Kretschmer, R., Gerbig, C., Karstens, U., & Koch, F. (2012). Error characterization of CO₂ vertical mixing in the atmospheric transport model WRF-VPRM. *Atmospheric Chemistry And Physics*, 12(5), 2441-2458. <https://doi.org/10.5194/acp-12-2441-2012>
- Kshudiram, S. (2008). *The Earth's Atmosphere* [Ebook] (1st ed., pp. 9-21). Springer Berlin. Retrieved 15 June 2022, from <https://doi.org/10.1007/978-3-540-78427-2>.
- Mayer, B., Emde, C., Buras, R., & Kylling, A. (2012). *Radiative Transfer: Methods and Applications* [Ebook] (1st ed., pp. 55-67). In: Schumann, U. (eds) Atmospheric Physics. Research

Topics in Aerospace. Springer, Berlin, Heidelberg. Retrieved 14 September 2022, from https://doi.org/10.1007/978-3-642-30183-4_24

Merten, A., Tschirter, J., & Platt, U. (2011). Design of differential optical absorption spectroscopy long-path telescopes based on fiber optics. *Applied Optics*, 50(5), 738. <https://doi.org/10.1364/ao.50.000738>

Odintsova, T., Fasci, E., Moretti, L., Zak, E., Polyansky, O., & Tennyson, J. et al. (2017). Highly accurate intensity factors of pure CO₂ lines near 2 μm. *The Journal Of Chemical Physics*, 146(24), 244309. <https://doi.org/10.1063/1.4989925>

Okajima, H., Kakumal, S., Uchida, K., Wakimoto, Y., & Noda, K. (2006). Measurement of methane gas concentration using an infrared LED. In *2006 SICE-ICASE International Joint Conference* (p. 1). Busan; IEEE Xplore. Retrieved 14 September 2022, from <https://ieeexplore.ieee.org/document/4109236>.

Ponater, M., Dietmüller, S., & Sausen, R. (2012). *Greenhouse Effect, Radiative Forcing and Climate Sensitivity* [Ebook] (1st ed., pp. 85–100). In: Schumann, U. (eds) Atmospheric Physics. Research Topics in Aerospace. Springer, Berlin, Heidelberg. Retrieved 12 August 2022, from https://doi.org/10.1007/978-3-642-30183-4_6

Prineas, J., Olesberg, J., Yager, J., Cao, C., Coretsopoulos, C., & Reddy, M. (2006). Cascaded active regions in 2.4μm GaInAsSb light-emitting diodes for improved current efficiency. *Applied Physics Letters*, 89(21), 211108. <https://doi.org/10.1063/1.2392993>

Schrodin, M. (2018). *Laser Spectroscopy of Rubidium* (pp. 3-6). Karlsruhe: Karlsruhe Institute of Technology - Department of Physics.

Sha, M., De Mazière, M., Notholt, J., Blumenstock, T., Chen, H., & Dehn, A. et al. (2020). Intercomparison of low- and high-resolution infrared spectrometers for ground-based solar remote sensing measurements of total column concentrations of CO₂, CH₄, and CO. *Atmospheric Measurement Techniques*, 13(9), 4791-4839. <https://doi.org/10.5194/amt-13-4791-2020>

Siesler, H., Kawata, S., Ozaki, Y., & Heise, M. (2001). *Near-Infrared Spectroscopy: Principles, Instruments, Applications*. WILEY-VCH Verlag GmbH.

Skea, J., Shukla, P., Reisinger, A., Slade, R., Pathak, M., & Khourdajie, A. et al. (2022). *Climate Change 2022: Mitigation of Climate Change* (p. SPM-6). IPCC Sixth Assessment Report (AR6) - Working Group III of the Intergovernmental Panel on Climate Change. Retrieved from <https://www.ipcc.ch/report/sixth-assessment-report-working-group-3/>

Warneke, T., Petersen, A., Gerbig, C., Jordan, A., Rödenbeck, C., & Rothe, M. et al. (2010). Co-located column and in situ measurements of CO₂ in the tropics compared with model simulations. *Atmospheric Chemistry And Physics*, 10(12), 5593-5599. <https://doi.org/10.5194/acp-10-5593-2010>

Wei, P., Hsieh, Y., Chiu, H., Yen, D., Lee, C., Tsai, Y., & Ting, T. (2018). Absorption coefficient of carbon dioxide across atmospheric troposphere layer. *Heliyon*, 4(10), e00785. <https://doi.org/10.1016/j.heliyon.2018.e00785>